DEM analysis of passive failure in structured sand ground behind a retaining wall

Mingjing Jiang [1, 2, 3, 4,*], Maoyi Niu [1, 4], Wangcheng Zhang [5, 6]

[1]*Department of Geotechnical Engineering, College of Civil Engineering, Tongji University, Shanghai, China;*

[2]*Department of Civil Engineering, Tianjin University, Tianjin, China;*

[3]*State Key Laboratory for Disaster Reduction in Civil Engineering, Tongji University, Shanghai, China;*

[4]*Key Laboratory of Geotechnical and Underground Engineering of Ministry of Education, Tongji University, Shanghai, China;*

[5] *Department of Engineering, Durham University, Durham, UK;*

[6] *Institute for Geotechnical Engineering, ETH Zurich, Zurich, Switzerland*

**Corresponding author at: Department of Geotechnical Engineering, College of Civil Engineering, Tongji University, Shanghai 200092, China.*

E-mail: mingjing.jiang@tongji.edu.cn

Abstract

Assessment of active and passive earth pressures is of crucial importance in design of retaining structures. This paper aims to explore the progressive failure mechanism towards the passive state of natural sand ground, and to quantify the lateral earth pressure, resultant force and overturning moment on the retaining wall under both translational and rotational movement modes. A numerical modelling using the two-dimensional (2D) Discrete Element Method (DEM) is conducted with an advanced micro contact model considering the inter-particle bond strength of natural sand. Rankine theory based semi-analytical solutions of the lateral earth pressure and resultant force/moment have been proposed and compared with the numerical data. The results show that not only the wall movement mode but also the inter-particle bond strength has significant effects on the progressive formation of shear failure zone and mobilization characteristics of earth pressure. The larger the inter-particle bond strength is, the higher the lateral earth pressure can be mobilized, and hence more significant post-peak softening can be produced. The proposed solution can well describe the progressive mobilization of earth pressure towards the passive state and the post-peak softening state at rotational movement modes, potentially optimizing the design of retaining structures.

Key words: retaining wall; structured sand; passive earth pressure; Discrete Element Method; soil failure

1. Introduction

Assessment of active and passive earth pressures (i.e. earth pressures mobilized to the active / passive states as the retaining wall moves away from / towards the soil ground) against retaining structures, e.g. retaining walls, bridge abutments, anchor blocks, and sheet piles, is an important and classical problem in geotechnical and structural engineering [1, 2]. External factors that may result in translational or rotational movement of a retaining structure include surcharge loading, seismic activity, groundwater flow, etc. [3-5]. The distribution of earth pressure as well as the resultant force and moment on the retaining wall is closely associated with the characteristics of the retaining wall, such as the interface friction [6], movement mode [7-9] and displacement magnitude [10-14]. They also largely depend on the soil properties and surface inclination of backfills [15-20]. Three main types of retaining wall movement, i.e. translation (T), rotation about the bottom (RB), and rotation about the top (RT) of wall, and their combinations have been recognized [7, 9]. All above concerns make this classical problem of complexity and remain an open issue in many aspects, though considerable attention has been paid.

Some classical analytical approaches, such as the Rankine, Coulomb, and log-spiral theories, have been used in practice and the literature, assessing the active and passive earth pressures and the critical slip surface [2, 21-25]. However, these analytical studies have mainly focused on the translational movement mode with limited attempts made on the rotational movement modes [26]. In addition, the progressive mobilization of earth pressure and its effect on the resultant force on the retaining wall have not been fully understood and considered in most analytical approaches. Some pioneering investigations on the displacement-dependent evolutions of earth pressure towards the active or passive state have been carried out during the last two decades [10, 11, 13, 27, 28]. Yet, the post-peak softening evolution of earth pressure on the retaining wall supporting a natural sand ground needs to be further explored to calculate the resultant force and moment correctly.

In addition to analytical studies, the earth pressure on the retaining wall and the wall response have been investigated and discussed via physical model tests [9, 29-33] and numerical modelling [34-38]. They have been mainly focused on cohesionless (or remoulded) backfills with very little addressing the active and passive failure of structured soils which are not seldom in practice, e.g., in deep excavations [14] and landslide mitigations. Due to sedimentary and loading histories, most natural soils are of bonding/cementing structures at the particulate level [39-40]. Consequently, structured [51, 52] (or cohesive /cemented [42] /bonded [50]) soils are usually equipped with somewhat cohesion and face strain softening during degradation. Although the cohesion effect has been early considered in the modified Rankine solution [41], its application has been limited to the translational movement (T) mode of retaining wall. A rotating retaining wall results in non-uniform displacements along the ground depth, which may cause the progressive failure of structured soil. Its effect on the gradual mobilization of earth pressure on the rotating retaining wall can be hardly revealed by the physical modeling because of the difficulty in preparing structured soil samples. The Discrete Element Method (DEM), which can simulate the micro scale bond structures [42-43], may provide an efficient tool to gap the problem.

This paper explores the passive failure mechanism from the microscopic view of point and the evolution of earth pressure from pre-peak to post-peak stages under both translational and rotational movement modes of retaining wall in natural sand ground by DEM. To investigate the effect of inter-particle bond structures of natural sands, an advanced bond contact model is employed in the DEM modelling. Based on the DEM investigations of translational mode and classical Rankine theory, an original semi-analytical solution is developed to assess the evolutions of resultant force and moment at the rotation modes, considering the displacement-dependent mobilization and post-peak softening characteristics of earth pressure. The proposed solution is expected to optimize the design of retaining structure, which needs further improvements to consider the realistic rough wall-soil interface and ‘soil arching’ effect.

2. Numerical details

2.1. Bond contact model for structured sand

A simplified 2D bond contact model based on Jiang et al. [44] was employed in this study. As observed from a scanning electron micrograph of natural sand [45], the formation of inter-particle bond structures requires a sufficiently small inter-particle gap. The critical gap, which is the maximum thickness of bonding materials, is denoted as h_{max}^{cr} here. With the presence of bond structures, the contact behaviours are jointly controlled by the particle surfaces (defined as the inter-particle contact) and the bonding materials (defined as the bond contact). They are briefed as follows.

The inter-particle contact, considering the rolling resistance [46], is activated once the two neighboring particles touch with each other (i.e. inter-particle gap h_{min} = 0, overlap between particles $u_n \geq 0$) or the inter-particle bond breaks. A linear elasticity is considered with the normal, tangential and rolling stiffness of particles being k_n^p, k_r^p and k_s^p, respectively; while the elasticity thresholds are controlled by the inter-particle frictional coefficient μ^p in the tangential direction and the inter-particle rolling resistance coefficient β^p in the rolling direction. The inter-particle mechanical response can be described as follows:

$$F_n^p = \begin{cases} k_n^p u_n, \ u_n \geq 0 \\ 0, \ u_n < 0 \end{cases}, \quad F_s^p \leftarrow \min[k_s^p \Delta u_s + F_s^p, \mu^p F_n^p], \quad M^p \leftarrow \min[k_r^p \Delta\theta + M^p, \frac{F_n^p \beta^p \bar{R}}{6}] \tag{1}$$

where F_n^p, F_s^p and M^p are normal force, shear force, and moment transmitted between particles, respectively; the rolling stiffness $k_r^p = k_n^p \left(\beta^p \bar{R}\right)^2 / 12$; Δu_s and $\Delta\theta$ are the incremental relative shear displacement and rotational angle, respectively.

The bond contact behaviours, on the other hand, are governed by the bond contact model accounting for bond rolling resistance. The bond rolling resistance coefficient β^b is related to the dimensions of bonding materials and given by [44]

$$\beta^b = \frac{\sqrt{4\bar{R}^2 - (2\bar{R} + h_{min} - h_{max}^{cr})^2}}{\bar{R}} \tag{2a}$$

where $\bar{R} = \dfrac{2R_1R_2}{R_1 + R_2}$ is the average radius of the two particles of radii R_1 and R_2, respectively. For the bond contact, the thresholds in the normal, tangential and rolling directions are denoted by F_n^b, F_s^b, and M^b, respectively; and they are limited by an ellipsoid in the F_n^b - F_s^b - M^b space (i.e. the red envelop in Fig. 1). For each F_s^b - M^b cut plane normal to the F_n^b axis, an elliptic envelope can be given by

$$\left(\frac{F_s^b}{R_{sb}}\right)^2 + \left(\frac{M^b}{R_{rb}}\right)^2 = 1 \quad \text{(critical state)} \tag{2b}$$

where R_{sb} and R_{rb} represent the shear strength and rolling strength of bond, respectively, which depend on the normal bond force F_n^b, compressive bond capacity R_{cb}, tensile bond capacity R_{tb} and critical bond thickness h_{max}^{cr}, given by

$$R_{sb} = \mu^b \cdot R_{cb} \cdot \frac{F_n^b + R_{tb}}{R_{cb} + R_{tb}} \cdot \left[1 + g_s \cdot (\ln \frac{R_{cb} + R_{tb}}{F_n^b + R_{tb}})^{f_s}\right], \quad R_{rb} = \frac{\bar{R}\beta^b R_{cb}}{6} \cdot \frac{F_n^b + R_{tb}}{R_{cb} + R_{tb}} \cdot \left[1 + g_r \cdot (\ln \frac{R_{cb} + R_{tb}}{F_n^b + R_{tb}})^{f_r}\right] \tag{2c}$$

where f_s, g_s, f_r, g_r are fitting parameters [44]. Before reaching the force/moment limits, simple linear-elastic relationships are assumed in each direction with the constant elastic modulus of bond denoted by E^b. Once broken, the remaining bond materials attached to the individual particles may still contribute to inter-particle behaviours as long as they are in contact with each other (i.e. $F_n^b > 0$ upon compressive breakage). The corresponding residual bond strengths are denoted by $F_{n,resid}^{b}$, $F_{s,resid}^{b}$, and M_{resid}^{b}, respectively, which depend on the magnitudes of F_n^b, β^b and frictional coefficient of bond μ^b. Upon tensile breakage, however, the broken bond materials attached to each particle are separated, and thus the residual bond strength falls to zero in each direction. The residual envelope is highlighted in blue in Fig. 1. The mechanical response of bond can be expressed as follows:

$$F_n^b = \begin{cases} k_n^b\left(u_n - u_0\right), \ -R_{tb} < F_n^b < R_{cb} \\ F_{n,resid}^b = \lambda R_{cb}, \ F_n^b \geq R_{cb} \\ 0, \ F_n^b \geq -R_{tb} \end{cases}, \quad F_s^b = \begin{cases} k_s^b \Delta u_s, \ F_s^b < R_{sb} \\ F_{s,resid}^b = \mu^b F_n^b, \ F_s^b \geq R_{sb} \text{ and } F_n^b > 0 \\ 0, \ F_s^b \geq R_{sb} \text{ and } F_n^b \leq 0 \end{cases},$$

$$M^b = \begin{cases} k_r^b \Delta\theta, \ M^b < R_{rb} \\ M_{resid}^b = \dfrac{F_n^b \beta^b \bar{R}}{6}, \ M^b \geq R_{rb} \text{ and } F_n^b > 0 \\ 0, \ M^b \geq R_{rb} \text{ and } F_n^b \leq 0 \end{cases} \tag{2d}$$

where u_0 is the initial overlap at the formation of bond, k_n^b, k_s^b and k_r^b are the normal, shear and rolling stiffness of bond respectively which can be calculated by E^b. In summary, the bond contact behaviours are controlled by parameters including R_{cb}, R_{tb}, μ^b, E^b and h_{max}^{cr}, and more details about the bond contact can be referred to Jiang et al. [44].

2.2. Parameters and properties of sand

Four types of sand are considered in the study: pure sand (i.e. cohesionless or reconstituted sand) and structured sand (i.e. cohesive/cemented/bonded sand) I/II/III. Their main micro parameters are given in Table 1, which would be used in both the simulated biaxial compression tests and subsequent boundary-value modelling. The parameters of inter-particle contact are the same in all the cases. This ensures that the residual strengths of structured sands approach the pure sand, though minor difference is expected as the remaining bond materials attached to individual particles may still work when broken (as presented later in Fig. 2c). Regarding the bond contact parameters, the compressive and tensile bond strengths (i.e. R_{cb} and R_{tb}) are varied among cases to simulate different cementation levels while the other bond parameters remain the same, as listed in Table 1.

To calibrate their macro mechanical properties, a series of numerical biaxial compression tests were performed, and details can be referred to the Appendix. On this basis, the apparent cohesion c and peak (residual) internal friction angle φ (φ_r) can be obtained, which fall in the range of practical cemented sands [53], as illustrated in Table 1. The apparent cohesion of the structured sands increases significantly with the increase of bond strength and is valued at 25.2 kPa, 44.7 kPa, and 62.5 kPa for structured sand I/II/III, respectively. The peak and residual internal friction angles, however, increase slightly with bond strength, and remain almost a constant ranging 30.21°~31.73° and 23.87°~25.42° respectively.

2.3. Generation of ground and set of retaining wall

The structured sand ground was generated by the following steps.

- Using the multi-layer under-compaction method [47], the sand ground was first generated by compacting eight layers of particles to the target void ratio e of 0.27, and its final size was 6 m × 2.75 m (width × height), as presented in Fig 2.
- The generated ground was then consolidated with an amplified gravity level of 5g in a spirit of centrifuge physical modelling, and thus the prototype of sand ground is 30 m × 13.75 m and the retaining wall is 10 m high.
- The inter-particle bond behaviours were finally assigned to the certain real/visual contacts with their inter-particle gaps less than the critical value.

The ground was composed of 298,550 particles with the scaled particle size distribution given in Fig. 16a, and there were 711,797 bond contacts at the initial state. The particle diameters range from 6 mm to 9 mm with the mean value d_{50} of 7.6 mm. A rigid retaining wall of h = 2 m in height was used to sustain the ground, with an additional wall element of 0.2 m set above to avoid flowing over of particles during the movement of the retaining wall. The size effect of d_{50} value on the earth pressure and its resultant force can be effectively eliminated as long as d_{50}/h < 1/200 is satisfied [57], and here d_{50}/h was set to be about 260 which is sufficiently small. In addition, the ground below the bottom of retaining wall is 0.75 m in depth, which is sufficient to eliminate any boundary effect. The wall-soil interface was set to be smooth here as assumed in the Rankine theory, so that a direct comparison between numerical results and Rankine solutions can be made. To track key field parameters during the wall movement, 57 $\times$25 global measurement circles were placed uniformly across the sand ground. The size of measurement circle was chosen such that it was sufficiently large to ensure a representative elementary volume but not to lose localised features. Here the radius of each measurement circle was taken as 75 mm (i.e., around 19 times d_{50}), containing about 320 particles, and it moves with the particle located closest to the circle center.

Three basic retaining wall movement modes, i.e., T, RB, and RT modes, were simulated, as presented in Fig. 2. The translational and angular velocities of the retaining wall were set to be small sufficiently as $\dot{u} = 7 \times 10^{-4}$ m/s and $\dot{\theta} = 7 \times 10^{-4}$ rad/s, respectively. Such that, the 2D inertia number quantifying the dynamic effects is $I = \dot{\varepsilon}\sqrt{m/p} = 4.3 \times 10^{-5} << 1$ (where $\dot{\varepsilon}$, m and p denote the shear strain rate, mass of sand ground and confining pressure respectively; average values of later numerical results have been adopted), ensuring that the DEM simulations were performed under quasi-static conditions [48]. In the following analysis, the lateral displacement is denoted by s. It is constant along the wall depth at the T mode, but various at the RB and RT modes with the average located at the wall center and denoted by s_{avg}. Hence, the normalized average lateral displacement s_{avg}/h (h = 2 m) is equal to $s/2$ at the T mode and $\theta / 2$ (where θ represents the rotation angle of the wall) at the RB and RT modes, respectively.

3. Numerical results

3.1. Passive failure mechanism of structured sand ground

In this section, the passive failure mechanism is investigated under different movement modes of the retaining wall for all four types of sand grounds.

3.1.1. Characteristics of shear band formation

The bond breakage ratio, defined as the ratio of the broken bond number to the initial bond number, can be used to analyze the progressive formation of localized shear zone in structured sands [42]. Fig. 3 shows the evolutions of the bond breakage ratio for all structured sand cases. Regardless of the inter-particle bond strength, at the T and RT modes, the bond breakage ratio grows rapidly until it approaches a asymptotic steady value with the increase of the retaining wall displacement, corresponding to the formation of an unique shear band (as given later in Fig. 4). By contrast, the growth of bond breakage ratio at the RB mode is much slower and more gentle than the other two modes, corresponding to the successive formation of several parallel shear bands (as depicted later in Fig. 4). For structured sand cases I and II, it can be observed that the steady bond breakage ratio is the smallest at the RT mode while the largest at the T mode till the end of the simulation (s_{avg}/h increases to 7%); however, the latter is expected to be surpassed by the RB mode with further wall displacement as observed in structured case III. For each movement mode, the larger the bond strength is, the smaller the steady bond breakage ratio is.

The features of evolved localized shear zone (i.e. shear band) are further visualized with the contours of shear strain in Fig. 4. Some major features are described below.

- For the retaining wall under the T mode, the development of shear strain is generally uniform over the whole shear band though it is slightly more concentrated at the wall bottom. As the value of s_{avg}/h approaches the critical (around 3%, which will be discussed later in section 3.2), a straight shear band becomes apparent showing the planar wedge failure mechanism (i.e. the Coulomb mechanism). With the further increase of s_{avg}/h, the shear strain within the shear band grows continually, making the rupture surface more significant.

- For the retaining wall under rotation modes, the shear strain is initially localized near the wall bottom and wall top for the RT and RB modes, respectively. At a later stage, a distinct curved shear band gradually propagates upwards to the ground surface at the RT mode, showing a log-spiral failure mechanism. Rather than a distinct and unique shear band found at other movement modes, there are several parallel shear bands developing from the ground surface to the wall back at the RB mode.
- For each movement mode, the strain localization is more significant (concentrated) in the sand ground with the larger bond strength (or apparent cohesion), as shown in Fig. 4b. While the geometry features of the shear failure zone is independent of the bond strength. The ratio of shear band width to the average particle diameter d_{50} is approximately 20~30 at each mode, which is large enough to obtain reliable information within the shear bands [42]. At the T mode, the plane shear failure surface in the pure sand ground is inclined at around $(\pi/4-\varphi/2)$ to the horizontal as proposed by Rankine, while its inclination in structured sands is slightly larger than the theoretical solution, as depicted in Fig. 4b.
- The characteristics of shear failure zone at each movement mode in four sand cases observed from the numerical modeling are similar to those emerging in dense pure sand investigated from experimental tests by Niedostatkiewicz et al. [32] (Fig. 4c), except for the slight discrepancy of T mode. It should be noted that, compared with the practical rough wall surface,

the assumption of smooth wall-soil interface limits the development of the accompanied radial localized shear zone from wall top observed in Fig. 4c. The similar phenomenon of missing radial shear zone in a smooth wall case at the T mode was also investigated by Benmeddour et al. [19], Guo and Zhao [58], and Altunbas et al. [59], as illustrated in Fig. 4d. Moreover, as the roughness of wall-soil interface increases, the main shear zone connecting wall toe with top free surface for the T mode changes from linear to curvilinear geometry.

More details of the shear band development under various retaining wall movement modes can be revealed through the investigations of the force chains and the contours of void ratio, bond breakage ratio, average pure rotation rate (i.e. APR) and soil displacement. Fig. 5 presents these details for the structured sand I case with s_{avg}/h = 5.25%. Among them, the contours of void ratio, bond breakage ratio and APR (as given in Figs. 5a, 5b and 5c) are obtained based on the average value measured in each global measurement circle, and the detailed calculations are given as follows, as referred to [42, 60]. The void ratio in each measurement circle is calculated by $(S - S_p)/S_p$, where S is the area of a measurement circle and S_p is the total area of particles within the circle. The bond breakage ratio is calculated as $N_b - N_r / N_b$, where N_b and N_r represent the number of bond at the initial state and a certain s_{avg}/h respectively within each circle. The APR is defined as $\frac{1}{N}\sum_{k=1}^{N}\left[\frac{1}{r^k}\left(\dot{\theta}_1^k r_1^k + \dot{\theta}_2^k r_2^k\right)\right]$, where N is the number of contacts in a measurement circle, r_i^k and $\dot{\theta}_i^k$ (i = 1, 2) are the radii and rotation rates of the two discs forming the k^{th} contact, and $r^k = 2r_1^k r_2^k / (r_1^k + r_2^k)$ is the average radius. The positive and negative APR in Fig. 5c represent the anticlockwise and clockwise rotation of grains, respectively. It can be seen that, the void ratio, bond breakage ratio, and soil particle rotation inside the shear band are all significantly larger than those outside the band, representing the volumetric dilation and concentrated energy dissipation inside the band. The disturbed zone at the passive failure state can be clearly observed through the displacement field as shown in Fig. 5d. The vector arrows in the displacement field are assigned with colors according to the relative magnitudes of particle displacements, as grouped in the color scale on the right sides of the figures. Compared with the T mode, the disturbed zone is much narrowed at the RB mode but slightly enlarged at the RT mode with a curved boundary. Different from the pure sand case, the input energy tends to be dissipated more intensively not only through the grain rearrangement but also through the bond breakage inside the shear band in structured sand cases. In Fig. 5e, the compressive and tensile contact forces are marked as black and red lines, respectively, with the line thickness being proportional to the magnitude of contact force. Compared with the compressive contact forces, the tensile contact forces are far smaller and hence the red lines can be only observed with an enlarged view. As expected, within the main localized shear zones, the force chains are relatively sparse for the sand dilatancy and most of the stronger ones gradually rotate so that their preferred directions tend to be perpendicular to the retaining wall or the shear bands (see Fig. 5e), which is in agreement with the observation by Nikta et al. [37]. In the triangle region between retaining wall and shear zone, the strong force chains mainly develop along the inclination of linear/curved shear zone at the T/RT mode, and those of RT mode distribute more non-uniformly with depth implying a significant stress redistribution behind the retaining wall.

3.1.2. Stress path inside the shear band

The evolution of stress status (or the stress path) inside the shear failure zone is monitored and discussed in this subsection, taking the structured sand I case as an example. A series of local measurement circles with the same radius of 75 mm as global ones, as representative element volumes, were placed inside the shear band prior to the simulation, as illustrated in Fig. 6. The mean stress and deviatoric stress are calculated as $p=\frac{\sigma_1+\sigma_3}{2}=\frac{\sigma_x+\sigma_y}{2}$ and $q=\frac{\sigma_1-\sigma_3}{2}=\sqrt{\left(\frac{\sigma_x-\sigma_y}{2}\right)^2+\tau_{xy}^2}$, respectively (where σ_1 and σ_3 are the major and minor principal stresses, respectively, σ_x and σ_y are the horizontal and vertical stresses, respectively, and τ_{xy} is the shear stress on the plane normal to the horizontal direction). In Fig. 6, the strength envelopes are plotted based on the elementary testing results (as listed in Table 1, and see Appendix). K_0 lines are given by $K_0=1-\sin\varphi$ where the frictional angle is also determined from the elementary tests. It can be seen that, in this case, both the initial and failure points of the boundary value problem fall at the analytical lines with parameters from the elementary tests, suggesting the macro properties of granular soils from designed elementary tests are applicable to the boundary value problem studied here.

The stress path starts at a point (which depends on the stress level and hence the depth of interest) of the K_0 line, and then moves towards the mean stress axis, representing the decrease of the deviatoric stress. It owes to that the horizontal stress which initially acts as the minor principal stress gradually grows and surpasses the vertical stress becoming the major principal stress. With the increase of the retaining wall displacement or rotation angle, the horizontal stress is further mobilized, making both the mean and deviatoric stresses increase continuously. Those stress paths are all limited by the peak strength envelope at the critical displacement of the retaining wall (literately, the passive failure state). Thereafter, the stress paths drop towards the residual strength envelope accompanied by the shear band formation.

To sum up, the geometry features of the shear failure zone mainly depends on the retaining wall movement mode, while the degree of shear strain localization tends to increase with the bond strength (cohesion) of sand ground. The progressive formation of shear band, especially in the structured sand grounds, can be well captured by the DEM micro scale information, e.g. the bond breakage ratio, APR, void ratio, force chains and stress path.

3.2. Evolution of lateral earth pressure and resultant force

In this section, the evolutions of distributed lateral earth pressure and the resultant force during the retaining wall movement are discussed for all cases, addressing the effects of the wall movement mode and inter-particle bond strength.

3.2.1. Distribution of lateral earth pressure

To analyze the effect of inter-particle bond structures of sand grounds on the lateral earth pressure, two cases: pure sand and structured sand I, under the basic movement mode (i.e. T mode) are selected. The distributions of lateral earth pressure at different stages for the two cases are provided in Fig. 7. The theoretical at-rest earth pressure σ_0 and the modified Rankine solution of passive earth pressure σ_p considering the cohesion effect [41] are also presented for comparison. They are given by

$$\sigma_0 = \gamma z K_0 \tag{3}$$

$$\sigma_p = \gamma z K_p + 2c\sqrt{K_p} \tag{4}$$

respectively, where z is the depth, γ is the soil unit weight, and $K_p = \tan^2\left(\pi/4 + \varphi/2\right)$ (φ corresponds to the peak internal friction angle given in Table 1) is the passive earth pressure coefficient. At the initial K_0 state, the measured lateral earth pressure has a good agreement with the theoretical solution (Eq. (3)). Due to the identical translational displacement along the wall depth, the soils behind the retaining wall are mobilized uniformly at the T mode. Consequently, the lateral earth pressure σ_h tends to distribute linearly along the retaining wall independently of s_{avg}/h. The peak lateral earth pressure σ_p at the passive state is therefore mobilized almost simultaneously along the wall depth regardless of the soil cohesion, which evidences the Rankine assumption. The finding about simultaneous mobilization of σ_h in pure sand behind the retaining wall moving at the T mode has also been revealed experimentally by some other studies (e.g. Fang et al. [9]). This conclusion is extended to the structured sands in the study. Note that, the critical s_{avg}/h is defined as the s_{avg}/h at the passive (peak) state of the lateral earth pressure σ_p (or the peak resultant force E_p). As observed from Fig. 7, the critical s_{avg}/h to the passive state of σ_h is about 4% ~ 5% in the pure sand case, which falls in the empirical range summarized by Clough and Ducan [1] and Zhang et al. [28]. In the structured sand I case, however, it is a bit smaller at around 3%. Note that, the value of critical s_{avg}/h is affected by the wall-soil interface friction and other granular properties in addition to the cohesion [9, 15]. Moreover, the distinct post-peak softening behavior of the lateral earth pressure can be observed in the structured sand I case, which is absent in the hardening pure sand. For the structured sand cases, the lateral earth pressure σ_h gradually decreases to the residual value σ_r with the further increase of s_{avg}/h, which approximates the passive earth pressure σ_p of the pure sand case calculated by Eq. (4) with c = 0. Generally, the lateral earth pressure at the post-peak stage also remains linearly distributed along the depth though slight non-uniformity is exhibited during its declination.

Regarding the rotation modes, nonlinear distribution of lateral earth pressure along the depth is apparent in the structured sand case indicating the non-uniform mobilization of soils behind the retaining wall, which is similar to the pure sand case. As shown in Fig. 8, at the RB mode, the lateral earth pressures near the wall toe are far less mobilized than those at shallow depths and the soils may not reach the passive failure state in theory. While at the RT mode, the soils near the wall toe are more quickly mobilized to the passive state with the lateral earth pressure close to the Rankine solution, compared to the less mobilized counterparts near the wall top. Such that, only a portion of the soils behind the retaining wall can be fully mobilized to the passive state at the rotation modes, which is expected to decrease the peak resultant force E_p acting on the retaining wall. Moreover, the early mobilized soils may enter the post-peak softening stage when the later mobilized soils just approach or still far below the peak, further reducing the peak resultant force on the wall.

It can be clearly observed from the figures that, the classical Rankine solution can predict the passive earth pressure only for the T mode, which needs to be adjusted to account for a) the non-uniform mobilization of soils behind a rotating retaining wall, and b) strain softening in structured sand ground. Note that the progressive growth of lateral earth pressure σ_h before reaching the passive state and its post-peak softening in structured sand cases are essentially related to the lateral displacement s behind the retaining wall. This is supported by the following facts, as observed in Fig. 8.

- Although the critical s_{avg}/h (or critical θ) required to achieve the peak lateral earth pressure σ_p is observed to be different along wall depth under the rotation modes (e.g. around 1% ~ 2% near the wall top at the RB mode or the wall toe at the RT mode, and approximately 3% behind the central point of the retaining wall for the both modes), the values of s/h basically coincide with the critical s_{avg}/h (i.e. around 3% as aforementioned) observed at the T mode.
- Except for the portions near the rotation center, the lateral earth pressure σ_h along the rotating wall exhibit somewhat softening, which is in accordance with the post-peak behavior at the T mode.

In addition, Fig. 9 compares the lateral earth pressure distributions at certain values of s_{avg}/h for all cases. As shown in the figure, the general findings obtained from the structured sand I case are also valid for the other two structured sand cases, though the earth pressure magnitude and distribution curvature vary among cases. For each displacement mode, the larger the bond strength is, the higher the lateral earth pressure can be mobilized and hence more significant post-peak softening can be produced.

3.2.2. Evolution of resultant force and action point

The reaction force directly measured from the retaining wall should be balanced by the integration of the earth pressure along the wall (i.e. the resultant force on the wall) in the quasi-static condition. Fig. 10 provides the evolutions of reaction force E_h in the structured sand I case for all three movement modes. The theoretical values of E_0 and E_p are also given for comparison. They can be derived from Eq. (3) and (4), given by

$$E_0 = \frac{1}{2}\gamma h^2 K_0 \quad (5)$$

$$E_p = \frac{1}{2}\gamma h^2 K_p + 2ch\sqrt{K_p} \quad (6)$$

respectively. The mobilized peak cohesion and internal friction angle (i.e. c and φ) used in Eqs. (3)-(6) here were taken from the elementary test (as given in Table 1). This has been justified in Fig. 6 where the stress paths of soils behind the retaining wall during passive failure are well governed by the strength envelopes (as functions of c and φ) obtained from the elementary biaxial compression tests, though the actual mobilized cohesion and internal frictional angle to the passive state might be slightly different and governed by diverse factors, e.g., wall movement mode, wall roughness and soil types [6]. The consistency of mobilized soil properties in the two tests leads to the good agreement between the DEM and analytical (Eqs. (4) and (6)) results of lateral earth pressure σ_h and its resultant force E_p at the passive state for the T mode, as presented in Figs. 7 and 10. As shown in Fig. 10, the curves of E_h against s_{avg}/h at the T and RT modes show notable softening tendency, while hardening trend is recognized at the RB mode. The simulated peak reaction force E_p at the T mode is just about 5% smaller than the Rankine solution given by Eq. (6), while the values at the rotation modes are nearly 15% smaller than the Rankine solution. Note that, the trend of E_h and its peak value E_p mainly depend on the earth pressures acting at the bottom segment of wall because of the higher stress level there, which are significantly affected by the ‘soil arching’ (as stated later in section 4.2). Hence, for the RT mode, the post-peak softening behaviors of the more quickly mobilized earth pressure σ_h near the wall bottom dominates the significant softening trend of E_h-s_{avg}/h. As the wall toe displacement is twice larger than the average at the wall center, a smaller (i.e. around 50%) critical s_{avg}/h of E_p can be observed at the RT mode than the T mode. At the RB mode, however, the wall toe displacement is relatively smaller than the critical value, and thus the post-peak decrease of the earlier mobilized σ_h at shallow depths is compensated by the later mobilized higher σ_h at the bottom segment of wall, leading to the hardening trend of E_h-s_{avg}/h.

Fig. 11 compares the reaction forces in all cases. Despite the bond strength, the trends (i.e. softening at the T and RT modes and hardening at the RB mode) of E_h observed from the structured sand I case are valid for the other structured sand cases. Due to the hardening trend of E_h-s_{avg}/h, a characteristic reaction force determined by the intersection of two linear trending lines [62] is chosen as a representative of the ‘peak’ value at the RB mode, as depicted in Fig. 11b. The peak reaction force E_p increases with the increase of bond strength despite the wall movement mode. The critical values of s_{avg}/h to the peak reaction force E_p (i.e. peak point in the softening E_h-s_{avg}/h at the T and RT modes, and bilinear failure point in the hardening E_h-s_{avg}/h at the RB mode) in the three structured sand cases fall in the range of 2.5%~3.5%, 1.5% ~ 2.0% and 1.0% ~1.5% for the T, RT and RB modes, respectively, which is due to their similar bond breakage evolution and shear band formation history as discussed earlier in the paper. Note that, for the T mode, the passive (peak) lateral earth pressure σ_p at different depths and the peak reaction force E_p are mobilized almost at the same critical s_{avg}/h (Figs. 7b and 11a). The critical s_{avg}/h to E_p is reached at the state when the passive earth pressure σ_p is mobilized near the wall toe and top, respectively, for the RT and RB modes (Figs. 8, 11b and 11c). Moreover, at the T mode, the residual reaction forces E_r of three structured sand cases all approach the peak reaction force E_p of the pure sand case (Fig. 11a), as a result of the soil reconstitution within shear bands. Though for structured sands the elementary tests provide consistent macro properties with the retaining wall boundary value problem, the stress-strain responses in the two scales are slightly different for the pure sand case, with the elementary test exhibiting slight strain softening (Fig. 16b) while the retaining wall test of T mode exhibiting hardening E_h-s_{avg}/h (Fig. 11a). This means the threshold values of the void ratio e (and thus relative density) for distinguishing strain hardening/softening behaviours might be different in the two scales, which has also been investigated by some other studies [15, 61]. However, the macro property of the pure sand, i.e., the frictional angle, is broadly the same in the two scales (as in Fig. 7a).

The action point of the reaction force is of great significance to assess the anti-overturning stability of a retaining wall. Fig. 12 presents the evolutions of the normalized action point of E_h given by y/h (where y is the distance from the wall toe to the action point of E_h) in all cases. For the pure sand case, y/h is always close to the theoretical value, i.e. 1/3, at the T mode while a bit higher around 0.47 at the RB mode and lower around 0.25 at the RT mode, respectively. In contrast, for the structured sand cases, the reaction force center y at the T mode firstly stays around $1/3h$ before reaching the passive state but then slightly drops, which is in accordance with the slightly non-uniform softening of lateral earth pressure along the wall depth, as evidenced in Figs. 7b and 9a. Note that, the slight non-uniformity during the post-peak stage of σ_h would be neglected for simplicity in the following analysis.

4. Assessment of passive force and overturning moment on rotating walls

4.1. Establishment of the semi-analytical solution

As noted above, the mobilization of the lateral earth pressure σ_h towards the passive state and its post-peak softening in structured sand cases essentially depend on the lateral displacement of different depths behind the retaining wall. As the lateral displacement of soils behind the wall is the same over the depth, the relationship between the reaction force and the lateral displacement at the T mode has been adopted as a cornerstone for the assessment of lateral earth pressure at the rotation modes. Moreover, at the T mode, the Rankine passive solutions with cohesion and non-cohesion can well describe the numerical peak and residual results, respectively, which are adopted in the proposed fitted solutions to the rotation modes to ensure a simple application.

To compare the numerical results with the Rankine solutions, the normalized numerical reaction force E_h/E_p (E_p is the Rankine passive resultant force) against s_{avg}/h is plotted at the T mode for all sand cases in Fig. 13a. The theoretical values of E_r/E_p for both cohesive and cohesionless sand cases are also given in the figure. The theoretical residual resultant force E_r in all sand cases can be given by the Rankine solution of E_p without cohesion (Eq. (6)), and hence $E_r/E_p = 1$ for the pure sand case as the hardening behavior is relevant. Note that, at the T mode, the numerical results of E_p and E_r in all cases are close to the Rankine solutions with the differences between 5% and 10%. Moreover, for a better fitting later, the curves of E_h/E_p - s_{avg}/h in structured sand cases at the T mode can be divided into two stages, i.e., the pre-peak stage (i.e. from the initial K_0 state to the passive state) and the post-peak stage (i.e. from the passive state to the residual state), separated at the critical s_{avg}/h (hereinafter denoted by s_{cri}^{p}/h). By contrast, only the pre-peak stage is relevant for the pure sand case.

On this basis, the relationships of numerical reaction force and lateral displacement at the T mode for both cohesive and cohesionless sand cases are fitted. To standardize the fitting process, the numerical reaction force E_h at the T mode is normalized as $\frac{E_h - E_0}{E_p - E_0}$ and $\frac{E_h - E_r}{E_p - E_r}$ (where E_0, E_p, and E_r are numerical results) for the pre-peak and post-peak stages, respectively. Meanwhile, the lateral displacement s_{avg} is normalized as $\frac{s_{avg}}{s_{cri}^p}$ and $\frac{s_{avg} - s_{cri}^p}{s_{cri}^r - s_{cri}^p}$ (where the parameter s_{cri}^r represents the value of s_{avg} achieving 95% reduction in $\frac{E_h - E_r}{E_p - E_r}$, as used in Zhang et al. [49]) for the pre-peak and post-peak stages, respectively. Such that, the normalized values can be forced to range between zero and unity. Figs. 13b and 13c give the scatters of the normalized numerical data and the exponential fitting curves for the pre-peak and post-peak stages, respectively. The best fit of all numerical data using the least squares method gives

$$\begin{cases} \dfrac{E_h - E_0}{E_p - E_0} = -e^{\left(-\alpha \frac{s_{avg}}{s_{cri}^p}\right)} + 1 & \begin{pmatrix} \text{pure sand} \\ \text{structured sand } (s_{avg} \le s_{cri}^p) \end{pmatrix} \\ \dfrac{E_h - E_r}{E_p - E_r} = e^{\left(-\beta \frac{s_{avg} - s_{cri}^p}{s_{cri}^r - s_{cri}^p}\right)} & \left(\text{structured sand } (s_{avg} > s_{cri}^p)\right) \end{cases} \quad (7)$$

for the pre-peak and post-peak stages, respectively. Note that, the fitting parameters α and β are problem specific and here valued at 3.91 and 2.97, respectively. Their values may change from case to case and can be determined through the resultant force - lateral displacement response under the T mode.

As the lateral earth pressure of different depths is considered to be mobilized uniformly at the T mode, the fitting curves of the normalized reaction force are expected to work for the normalized earth pressure as well, i.e.,

$$\begin{cases} \dfrac{\sigma_h - \sigma_0}{\sigma_p - \sigma_0} = -e^{\left(-\alpha \frac{s}{s_{cri}^p}\right)} + 1 & \begin{pmatrix} \text{pure sand} \\ \text{structured sand } (s \le s_{cri}^p) \end{pmatrix} \\ \dfrac{\sigma_h - \sigma_r}{\sigma_p - \sigma_r} = e^{\left(-\beta \frac{s - s_{cri}^p}{s_{cri}^r - s_{cri}^p}\right)} & \left(\text{structured sand } (s > s_{cri}^p)\right) \end{cases} \tag{8}$$

Where the two fitted parameters α = 3.91 and β = 2.97 are obtained, respectively, as in the Eq. (7), the lateral displacement s along the wall depth can be expressed as $s = \dot{\theta} tz$ and $s = \dot{\theta} t(h - z)$ (where t is the time) at the RT and RB modes, respectively. The Eq. (8) is determined by four basic parameters: the passive and residual earth pressures (i.e. σ_p and σ_r), and the critical lateral displacements to the peak and residual states (i.e. s_{cri}^p and s_{cri}^r). The σ_p and σ_r can be calculated based on the Rankine theory (Eq. (4)) with certain c and φ), while the s_{cri}^p and s_{cri}^r can be determined by the numerical results. As observed from Fig. 13a, the s_{cri}^p / h is about 3% to 5%, which here is set to 3.25% and 4.25% for the pure and structured sand cases, respectively. The s_{cri}^r / h is only relevant for the structured sand cases and set to 7.25% here. Note that, those four basic parameters can also be determined by other theoretical solutions, numerical modelling or physical tests for the T mode. In addition, the wall roughness has effects on both strain localization characteristics and mobilization of lateral earth pressure [19, 58], which has not been considered in the current study. Some caution should be taken in application of the developed prediction in a rough wall case as the same in using the (modified) Rankine solution, though the prediction based on a smooth wall is generally conservative.

4.2 Applications on the rotating wall cases

Based on the exponential fitted solution (Eq. (8)), the distributions of lateral earth pressure σ_h at different rotation angles of the retaining wall are assessed for the RB and RT modes. As shown in Figs. 14a and 14b, non-linear distribution of the lateral earth pressure can be reflected by the proposed solution. Specially, the earth pressure is less mobilized near the rotation center of the wall and reaches the peak or even post-peak softening stage near the other end of the wall. By integrating the lateral earth pressure along the wall depth, the reaction force E_h, action point, and overturning moment M_h can also be assessed. Figs. 14c and 14d compares the proposed solutions and numerical results of the evolved reaction force and overturning moment on the rotating retaining wall, taking the structured sand I case as an example. The exponential fitted predictions and numerical data of the peak reaction force E_p, action point y/h, and peak moment resistance M_p for all cases are also listed in Table 2. As observed, the proposed solution modified from the Rankine solution can well agree with the peak reaction force and overturning moment measured from the DEM modelling, with most of the difference less than 15%. The predicted peak reaction force is slightly higher than the numerical data. However, the predicted peak moment resistance is slightly smaller than the numerical data due to the smaller moment arm (i.e. from the reaction force point to the rotation center) predicted, indicating a conservative estimation.

The slight differences between the proposed solutions and the numerical results result from the inaccurate predictions of the lateral earth pressure σ_h at certain locations of the rotating wall, as presented in Figs. 14a and 14b. This can be mainly attributed to the significant stress redistribution by ‘soil arching’, whereby soils are more mobilized at some locations compensating less mobilized nearby areas, and the soil arching effect tends to be more significant in stronger sand grounds, as shown in Figs. 9b and 9c. This stress redistribution phenomenon, which dooms to add nonlinearity to the earth pressure distribution, is not reflected in the proposed solution and worth further analysis. Two facts can be revealed from the soil arching caused stress redistribution: a) it mainly affect the curvature of lateral earth pressure distribution as well as the post-peak hardening/softening extent of integrated reaction force E_h at RB/RT mode, but has little effect on the pre-peak E_h especially its peak value E_p, which is verified in Fig. 14 and Table 2. b) the action center of reaction force may leave further away from the wall rotation center and hence the overturning moment M_h is higher than the prediction.

Furthermore, the proposed displacement-controlled solution can be also used to assess the more practical movement modes of retaining wall, i.e. rotation about a point below the wall bottom (RBT) or above the wall top (RTT). As shown in Fig. 2, a parameter n is used to indicate the location of wall rotation center. The RBT and RTT modes become the RB and RT modes respectively as n equals 0, and become T mode as n approaches infinity. Here the two cases (one RBT and one RTT) were selected with n = 0.5 in each case to compare the DEM numerical results and the predictions by the proposed solution, are given in Fig. 15. Compared with RB (RT) mode, larger displacement is allowed near the wall toe (top) at the RBT (RTT) mode at the same s_{avg}/h, and thus the higher lateral earth pressure can be mobilized there, implying that the 'soil arching' effect is weakened. As a result, the nonlinearity of lateral earth pressure distribution (i.e. the non-uniformity of earth pressure mobilization) is declined, and the peak values of resultant force E_p and moment M_p tend to increase as the parameter n increases from 0 to 0.5 (Figs. 14 and 15), all of which can be well predicted by the proposed solution. Moreover, the slight softening tendency of E_h-s_{avg}/h at the RBT mode (as marked in Fig. 15c) can be also basically grasped by the prediction, indicating the gradual transition from rotation mode to T mode as n increases.

5. Conclusions

This paper has focused on the passive failure mechanism of the structured sand ground supported by a retaining wall under three basic retaining wall movement (i.e. translation - T, rotation about the bottom - RB, and rotation about the top - RT) modes. Semi-analytical solutions of the lateral earth pressure, resultant force and overturning moment on the rotating retaining wall have been proposed. The analysis has been conducted using the Discrete Element Method (DEM) with an advanced bond contact model for structured sand. The main conclusions can be drawn as follows.

As the retaining wall translates or rotates towards the passive failure state, strain localization within a band or multiple bands gradually becomes pronounced indicating the progressive formation of the rupture surface/surfaces, which is accompanied by soil dilation and concentrations of inter-particle bond breakage, particle rotation and shear displacement. The geometry characteristics of shear failure zone are largely affected by the retaining wall movement mode, while its localization extent is mainly related to the magnitude of bond strength. With a smooth wall-soil interface, the plane shear failure surface of the T mode in the pure sand case is inclined at around $(\pi/4-\varphi/2)$ to the horizontal as indicated in the Rankine theory, while its inclination in structured sand cases is slightly larger. The stress state within the shear failure zone evolves from the K_0 line to the peak strength envelope accompanied by the rotation of principal stress, and then drops to the residual state as the shear band forms.

Both the wall movement mode and the magnitude of bond strength (or cohesion) have significant effects on the evolution of lateral earth pressure as well as its resultant force. The lateral earth pressure σ_h with the increasing wall displacement exhibits a hardening response in the pure sand case, while a distinct post-peak softening response in the structured sand cases. The progressive mobilization of the lateral earth pressure to the passive state and its post-peak softening response in structured sands essentially depend on the lateral displacement of different depths behind the translating / rotating retaining wall. In structured sands, the passive (peak) lateral earth pressure σ_p at different depths and its peak resultant force E_p are mobilized almost at the same critical s_{avg}/h of around 2.5%~3.5% for the T mode, while for the RT (or RB) mode, the peak (or characteristic) E_p is reached at a smaller critical s_{avg}/h of around 1.5% (i.e. nearly 50% of the T mode) when the passive earth pressure σ_p is only mobilized near the wall toe (or wall top). The numerical results of lateral earth pressure σ_h and resultant force E_h at the peak and residual states for the T mode have a good agreement with the Rankine passive solutions. With the same movement mode, the larger the bond strength is, the higher the lateral earth pressure can be mobilized, and hence more significant post-peak softening can be produced.

Rankine theory-based solutions have been proposed to assess the resultant force and overturning moment on the retaining wall at the rotation modes, considering the displacement-dependent non-uniform mobilization of lateral earth pressure along the wall and its post-peak softening in the structured sand. Input parameters of the proposed method include the passive and residual earth pressures and their corresponding critical displacements. The former can be determined through the classical Rankine solutions and the latter can be obtained from numerical modelling or physical tests. The proposed method produces quite close predictions to the numerical results with respect to the peak reaction force and overturning moment. This warrants an optimization for design of retaining walls allowed to move rotationally.

The well predictions at the basic rotation (i.e. RB and RT) and more complex (i.e. RBT and RTT) modes demonstrate the solidarity of the proposed exponential fitted solution. Main shortages of the proposed solution include: a) the wall-soil interface is considered to be smooth to ensure the application of the Rankine theory; b) the soil arching effect can not be reflected, leading to inaccuracies of the earth pressure distribution, though which has been found to have little effect on the peak resultant force. Both issues worth further studies which however do not reduce the credibility of the semi-analytical framework proposed here.

The numerical results here could add contributions to the database of structured sands, and further comprehensive studies (including both numerical and physical tests, and considering more practical cases e.g. complex wall movements and wall roughness) are needed to solve the issue more systematically. The fitted solution was proposed based on the dimensionless numerical results and classical Rankine theory, which can provide a framework for future similar studies, and a careful validation is still suggested before any applications.

Appendix

A series of numerical biaxial compression tests were performed with a strain rate of 5%/min under five different confining pressures, i.e., 50 kPa, 100 kPa, 200 kPa, 400 kPa and 500 kPa. The grain size distribution is uniform in all specimens and provided in Fig. 16a in comparison with the Ottawa sand adopted by Wang and Leung [53]. To achieve computational efficiency, the DEM particles were enlarged by a certain scale maintaining almost the same grain size distribution curve with the realistic sands, as adopted in other studies [42, 43, 54, 55]. As has been investigated by [35-37], the magnitude of d_{50} would not make an appreciable difference to the strain localization patterns and the E_h-s_{avg}/h relationship, though a relatively large d_{50} can lead to a slightly increase of the shear band width and the peak resultant force E_p.

It can be seen from Figs. 16b-16e that, the numerical results can well capture the cementation effect on the mechanical properties of granular soils: a) the higher the cementation level, the higher the peak strength; b) the residual strength is almost independent of the cementation level. Moreover, the peak friction angles (30.21 °~ 31.73 °, as listed in Table 1) from the numerical modelling is rather comparable to the experimental values (28.6 °~ 32.1 °).

Acknowledgements

The research has been supported by the National Natural Science Foundation of China with Grant Nos. 51579178 and 51639008, which are all greatly appreciated.

References

1. Clough, G. W., Ducan, J. M.: Earth pressure. In Foundation engineering handbook. 2nd ed. Edited by Fang H Y. van Nostrand Reinhold, New York. 223-235 (1991)
2. Duncan, J. M., Mokwa, R. L.: Passive earth pressures: theories and tests. J. Geotech. Geoenviron. Eng. 127(3), 248-257 (2001)
3. Patki, M. A., Dewaikar, D. M., Mandal, J. N.: Numerical evaluation of passive earth-pressure coefficients under the effect of surcharge loading. Int. J. Geomech. 17(3), 06016024.1-06016024.15 (2017)
4. Hu, Z., Yang, Z. X., Wilkinson, S. P.: Analysis of passive earth pressure modification due to seepage flow effects. Can. Geotech. J. 55(5), 666-679 (2018)
5. Junied, B., Mohd, A. S.: A finite element performance-based approach to correlate movement of a rigid retaining wall with seismic earth pressure. Soil Dyn. Earthq. Eng. 114, 460-479 (2018)
6. Rowe, P. W., Peaker, K.: Passive earth pressure measurements. Géotechnique 15(1), 57-78 (1965)
7. Roscoe, K. H.: The influence of strains in soil mechanics. Géotechnique 20(2), 129-170 (1970)
8. James, R. G., Bransby, P. L.: A velocity field for some passive earth pressure problems. Géotechnique 21(1), 61-83 (1971)
9. Fang, Y. S., Chen, T. J., Wu, B. F.: Passive earth pressures with various wall movements. Journal of Geotechnical Engineering 120(8), 1307-1323 (1994)

10. Rao, K. S. S., Nayak, S., Choudhury, D.: Determination of displacement-related passive earth pressure. Geotechnical Engineering 35(2), 79-85 (2004)

11. Mei, G., Chen, Q., Song, L.: Model for predicting displacement-dependent lateral earth pressure. Can. Geotech. J. 46(8), 969-975 (2009)

12. Mei, G., Chen, R., Liu, J.: New insight into developing mathematical models for predicting deformation-dependent lateral earth pressure. Int. J. Geomech. 17(8), 06017003.1-06017003.5 (2017)

13. Tang, Y., Li, J. P., Ma, Y.: Lateral earth pressure considering the displacement of a rigid retaining wall. Int. J. Geomech. 18(11), 06018031.1-06018031.12 (2018)

14. Hu, H., Yang, M., Lin, P., Lin, X.: Passive earth pressures on retaining walls for pit-in-pit excavations. IEEE Access 7, 5918-5931 (2019)

15. Fang, Y. S., Ho, Y. C., Chen, T. J.: Passive Earth Pressure with Critical State Concept. J. Geotech. Geoenviron. Eng. 128(8), 651-659 (2002)

16. Hanna, A., Khoury, A. I.: Passive earth pressure of overconsolidated cohesionless backfill. J. Geotech. Geoenviron. Eng. 131(8), 978-986 (2005)

17. Tejchman, J., Bauer, E., Tantono, S. F.: Influence of initial density of cohesionless soil on evolution of passive earth pressure. Acta Geotech. 2(1), 53-63 (2007)

18. Shiau, J. S., Augarde, C. E., Lyamin, A. V. Sloan, S. W.: Finite element limit analysis of passive earth resistance in cohesionless soils. Soils Found. 48(6), 843-850 (2008)

19. Benmeddour, D., Mellas, M., Frank, R., Mabrouki, A.: Numerical study of passive and active earth pressures of sands. Comput. Geotech. 40, 34-44 (2012)

20. Vo, T., Russell, A. R.: Interaction between retaining walls and unsaturated soils in experiments and

using slip line theory. J. Eng. Mech. 143 (4), 04016120.1-04016120.12 (2017)

21. Luan, M., Nogami, T.: Variational Analysis of Earth Pressure on a Rigid Earth-Retaining Wall. J. Eng. Mech. 123(5), 524-530 (1997)
22. Soubra, A. H., Macuh, B.: Active and passive earth pressure coefficients by a kinematical approach. Geotechnical Engineering 155(2), 119-131 (2002)
23. Škrabl, S., Macuh, B.: Upper-bound solutions of three-dimensional passive earth pressures. Can. Geotech. J. 42(5), 1449-1460 (2005)
24. Xu, S. Y., Shamsabadi, A., Taciroglu, E.: Evaluation of active and passive seismic earth pressures considering internal friction and cohesion. Soil Dyn. Earthq. Eng. 70, 30-47 (2015)
25. Cai, Y. Y., Chen, Q. S., Zhou, Y. T., Nimbalkar, S. S.: Estimation of passive earth pressure against rigid retaining wall considering arching effect in cohesive-frictional backfill under translation mode. Int. J. Geomech. 17(4), 04016093.1-04016093.11 (2017)
26. Zhu, D. Y., Qian, Q. H., Lee, C. F.: Active and passive critical slip fields for cohesionless soils and calculation of lateral earth pressures. Géotechnique 51(5), 407-423 (2001)
27. Chang, M. F.: Lateral earth pressures behind rotating walls. Can. Geotech. J. 34(4), 498-509 (1997)
28. Zhang, J., Shamoto, Y., Tokimatsu, K.: Evaluation of earth pressure under any lateral deformation. Soils Found. 38(1), 15-33 (1998)
29. James, R. G., Bransby, P. L.: Experimental and theoretical investigations of a passive earth pressure problem. Géotechnique 20 (1), 17-37 (1970)
30. Milligan, G. W. E., Bransby, P. L.: Combined active and passive rotational failure of a retaining wall in sand. Géotechnique 26(3), 473-494 (1976)
31. Wilson, P., Elgamal, A.: Large-scale passive earth pressure load-displacement tests and numerical

simulation. J. Geotech. Geoenviron. Eng. 136(12), 1634-1643 (2010)

32. Niedostatkiewicz, M., Lesniewska, D., Tejchman, J.: Experimental analysis of shear zone patterns in cohesionless for earth pressure problems using particle image velocimetry. Strain 47(s2), 218-231 (2011)

33. Gutberlet, C., Katzenbach, R., Hutter, K.: Experimental investigation into the influence of stratification on the passive earth pressure. Acta Geotech. 8(5), 497-507 (2013)

34. Benmebarek, S., Khelifa, T., Benmebarek, N., Kastner, R.: Numerical evaluation of 3D passive earth pressure coefficients for retaining wall subjected to translation. Comput. Geotech. 35(1), 47-60 (2008)

35. Widulińsk, L., Tejchman, J., Kozicki, J., Leśniewska, D.: Discrete simulations of shear zone patterning in sand in earth pressure problems of a retaining wall. Int. J. Solids Struct. 48(7-8), 1191-1209 (2011)

36. Jiang, M. J., He, J., Wang, J. F., Liu, F.: Distinct simulation of earth pressure against a rigid retaining wall considering inter-particle rolling resistance in sandy backfill. Granul. Matter 16, 797-814 (2014)

37. Nitka, M., Tejchman, J., Kozicki, J., Leśniewska, D.: DEM analysis of micro-structural events within granular shear zones under passive earth pressure conditions. Granul. Matter 17(3), 325-343 (2015)

38. Kozicki, J., Tejchman, J.: Investigations of quasi-static vortex structures in 2D sand specimen under passive earth pressure conditions based on DEM and Helmholtz–Hodge vector field decomposition. Granul. Matter 19(2), 31 (2017)

39. Leroueil, S., Vaughan, P. R.: The general and congruent effects of structure in natural soils and

weak rocks. Géotechnique 40(3), 467-488 (1990)

40. Cuccovillo, T., Coop, M. R.: On the mechanics of structured sands. Géotechnique 49(6), 741-760 (1999)

41. Bell, A. L.: The lateral pressure and resistance of clay and the supporting power of clay foundations. Minutes of the Proceedings of the Institution of Civil Engineers. 199(1915), 306-336 (1915)

42. Jiang, M. J., Yan, H. B., Zhu, H. H., Utili, S.: Modeling shear behavior and strain localization in cemented sands by two-dimensional distinct element method analyses. Comput. Geotech. 38(1), 14-29 (2011)

43. Jiang, M. J., Zhang, W. C.: DEM analyses of shear band in granular materials. Eng. Comput. 32(4), 985-1005 (2015)

44. Jiang, M. J., Fu, C., Cui, L., Shen, Z. F., Zhu, F. Y.: DEM simulations of methane hydrate exploitation by thermal recovery and depressurization methods. Comput. Geotech. 80, 410-426 (2016)

45. Cuccovillo, T., Coop, M. R.: Yielding and pre-failure deformation of structured sands. Géotechnique 47(3), 491-508 (1997)

46. Jiang, M. J., Yu, H. S., Harris, D.: A novel discrete model for granular material incorporating rolling resistance. Comput. Geotech. 32(5), 340-357 (2005)

47. Jiang, M. J., Konrad, J. M., Leroueil, S.: An efficient technique for generating homogeneous specimens for DEM studies. Comput. Geotech. 30(7), 579-597 (2003)

48. Radjai, F.: Force and fabric states in granular media. AIP Conference Proceedings. Proceedings of the 6th International Conference on Micromechanics of Granular Media Golden, Colorado. 35-42 (2009)

49. Zhang, W., Wang, D., Randolph, M. F., Puzrin, A. M.: Catastrophic failure in planar landslides with a fully softened weak zone. Géotechnique 65(9), 755-769 (2015)

50. Jiang, M. J., Liu, J. D., Sun, Y. G., Yin, Z. Y.: Investigation into macroscopic and microscopic behaviors of bonded sands using the discrete element method. Soils Found. 53(6), 804-819 (2013)

51. Shen, Z. F., Jiang, M. J., Wang, S. N.: Static and kinematic damage characterization in structured sand. Acta Geotech. 14(8), 1403–1421 (2019)

52. Jiang, M. J., Hu, H. J., Liu, F.: Summary of collapsible behaviour of artificially structured loess in oedometer and triaxial wetting tests. Can. Geotech. J. 49(10), 1147-1157 (2012)

53. Wang, Y. H., Leung, S. C.: Characterization of Cemented Sand by Experimental and Numerical Investigations. J. Geotech. Geoenviron. Eng. 134(7), 992-1004 (2008)

54. Jiang, M. J., Zhu, F. Y., Liu, F., Utili, S.: A bond contact model for methane hydrate-bearing sediments with interparticle cementation. Int. J. Numer. Anal. Methods Geomech. 38, 1823-1854 (2014)

55. Jiang, M. J., Shen, Z. F., Zhu, F. Y.: Numerical analyses of braced excavation in granular grounds: continuum and discrete element approaches. Granul. Matter 15(2), 195-208 (2013)

56. Ding, X. B., Zhang, L. Y., Zhu, H. H.,Zhang, Q.: Effect of Model Scale and Particle Size Distribution on PFC3D Simulation Results. Rock Mech. Rock Eng. 47, 2139-2156 (2014)

57. Gudehus, G., Nuebel, K.: Evolution of shear bands in sand. Géotechnique 54(3), 187-201 (2004)

58. Guo, N., Zhao, J. D.: Multiscale insights into classical geomechanics problems. Int. J. for Numer. Anal. Methods Geomech. 40, 367-390 (2016)

59. Altunbas, A., Soltanbeigi, B., Cinicioglu, O.: DEM analysis of passive failure state behind a rigid retaining wall: effect of boundary conditions. E3S Web of Conferences 92, 14012 (2019)

60. Jiang, M. J., Yin, Z. Y., Shen, Z. F.: Shear band formation in lunar regolith by discrete element analyses. Granul. Matter 18(2), 1-14 (2016)

61. Jiang, M. J., He, J.: A distinct element analysis of critical state passive earth pressure against a rigid wall using a rolling resistance contact model. Rock and Soil Mechanics 36(10), 2996-3006 (2015) (in Chinese)

62. Hanna A, Khoury I A. Passive earth pressure of overconsolidated cohesionless backfill. J. Geotech. Geoenviron. Eng. 131(8), 978-986 (2005)

Table 1 Model parameters and target mechanical properties used in the DEM simulations

Parameters	Values			
	Pure sand	Structured sand I	Structured sand II	Structured sand III
Cohesion c [kPa]	0	25.2	44.7	62.5
Peak internal frictional angle φ [°]	30.21	30.86	31.59	31.73
Residual internal friction angle φ_r [°]	23.87	24.32	25.05	25.42
Particle density ρ [kg/m^3]	2600			
Inter-particle frictional coefficient μ^p	0.5			
Inter-particle rolling resistance coefficient β^p	1.4			
Normal contact stiffness of particle k_n^p [N/m]	2.0×10^8			
Tangential contact stiffness of particle k_s^p [N/m]	1.5×10^8			
Frictional coefficient of bond μ^b	/	0.5		
Critical bond thickness h_{max}^{cr} [m]	/	0.0013		
Elastic modulus of bond E^b [kPa]	/	2.5×10^5		
Tensile strength of bond R_{tb} [N/m]	/	6.0×10^4	8.6×10^4	1.1×10^5
Compressive strength of bond R_{cb} [N/m]	/	1.3×10^6	1.75×10^6	2.3×10^6
Frictional coefficient between wall and particle μ^w	0			
Normal contact stiffness of wall k_n^w [N/m]	1.5×10^9			
Tangential contact stiffness of wall k_s^w [N/m]	1.0×10^9			

Table 2 Comparisons between numerical and empirical results at the passive state for all cases

All cases of target sands		E_p [kN]			y/h of E_p		M_h by E_p [kN m]		
		DEM	Prediction	Difference	DEM	Prediction	DEM	Prediction	Difference
Pure sand	T	630.05	597.77	5.12%	0.343	0.337	/	/	/
	RB	415.07	442.56	6.62%	0.485	0.401	403.01	354.53	12.03%
	RT	574.57	579.46	0.85%	0.233	0.320	881.96	787.92	10.66%
Structured sand I	T	766.00	793.39	3.58%	0.366	0.373	/	/	/
	RB	575.77	617.07	7.17%	0.460	0.394	529.27	486.53	8.08%
	RT	699.97	722.75	3.25%	0.227	0.344	1082.22	948.33	12.37%
Structured sand II	T	896.00	945.21	5.49%	0.380	0.391	/	/	/
	RB	675.05	717.61	6.31%	0.456	0.423	615.95	607.56	1.36%
	RT	807.40	839.07	3.92%	0.222	0.351	1255.87	1089.42	13.25%
Structured sand III	T	1048.70	1074.90	2.50%	0.389	0.404	/	/	/
	RB	799.27	802.87	0.45%	0.433	0.420	691.86	674.30	2.54%
	RT	892.50	940.22	5.35%	0.206	0.360	1416.42	1203.41	15.04%

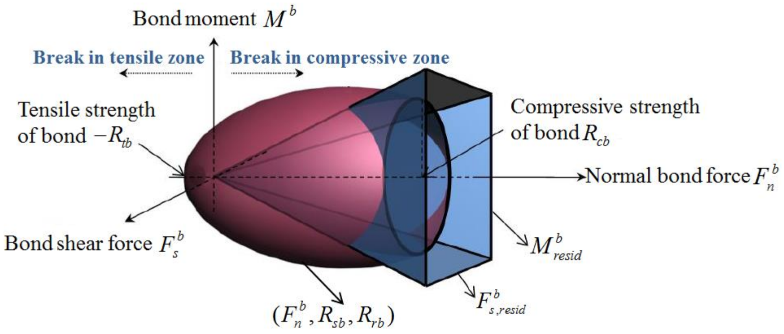

Fig.1 Bond strength envelope of the bond contact model [44]

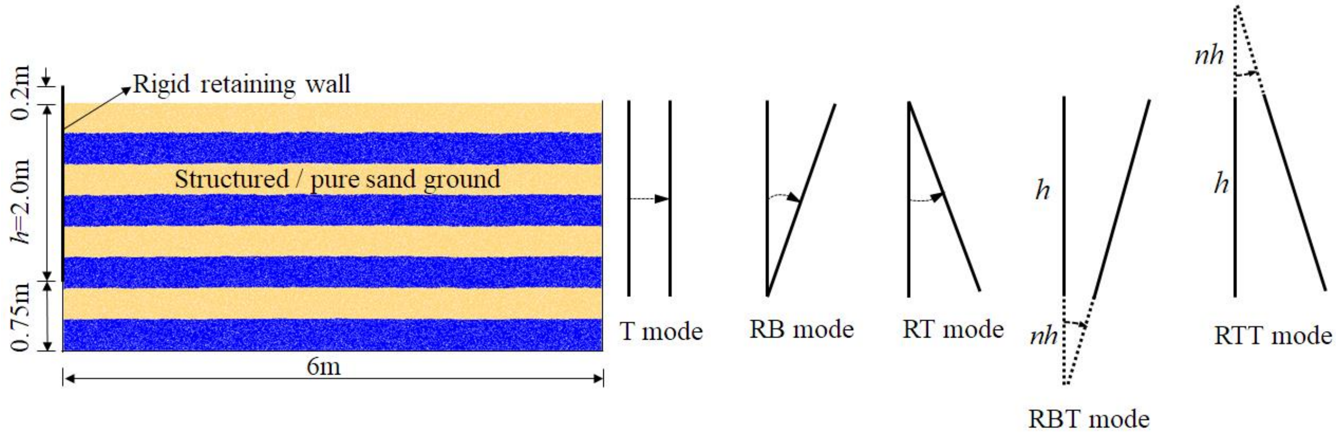

Fig.2 DEM modelling of sand ground with a rigid retaining wall and schematics of passive movement modes

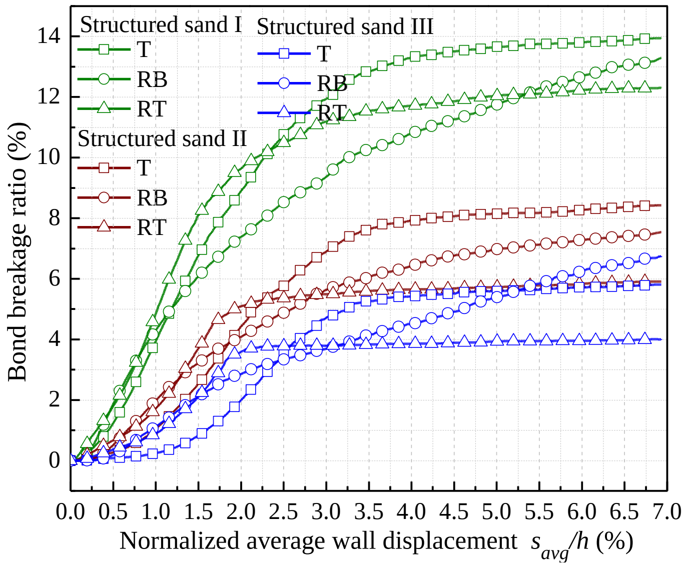

Fig.3 Evolution of bond breakage ratio against s_{avg}/h in all structured sand cases

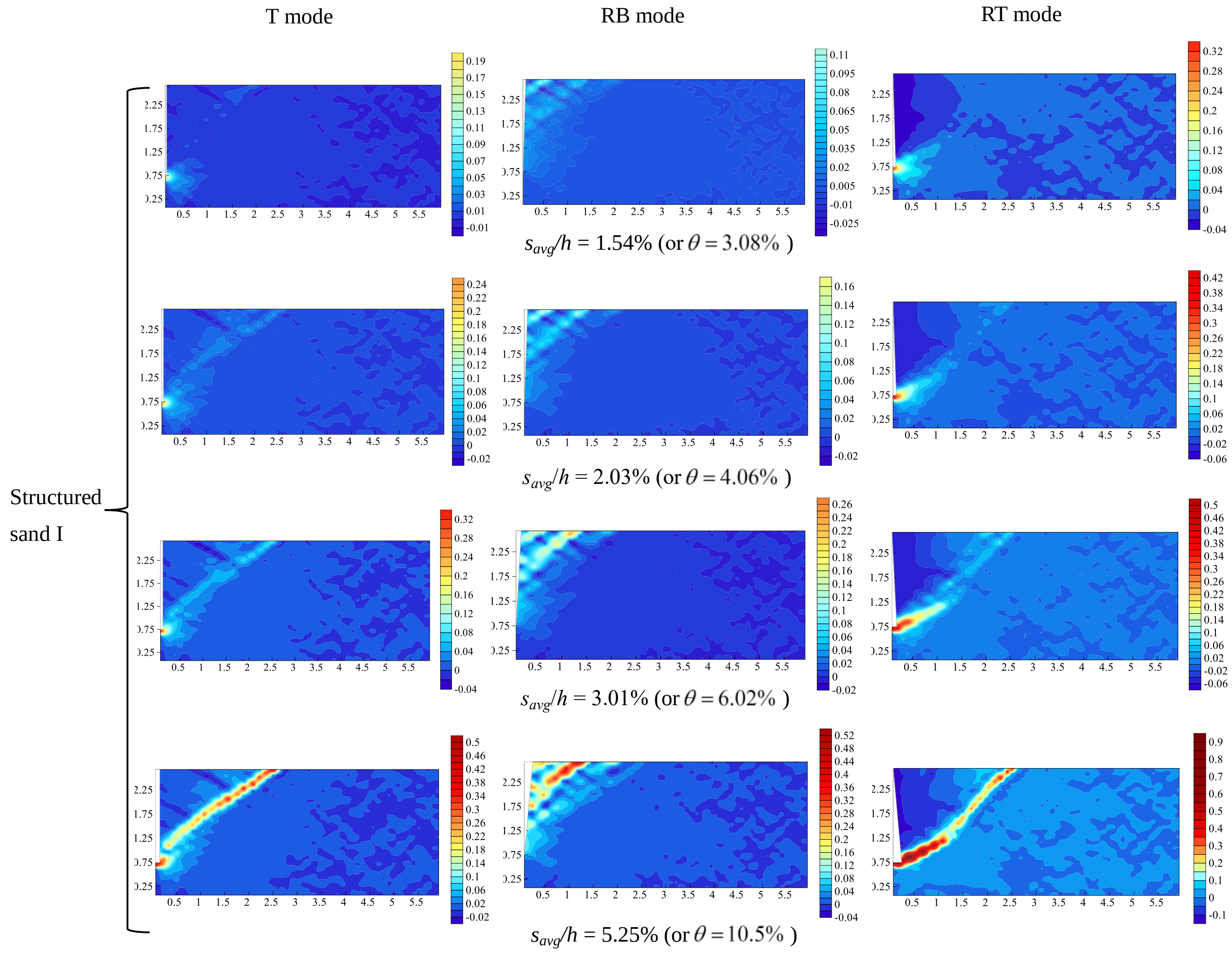

(a) Structured sand I case at the different s_{avg}/h by DEM modelling

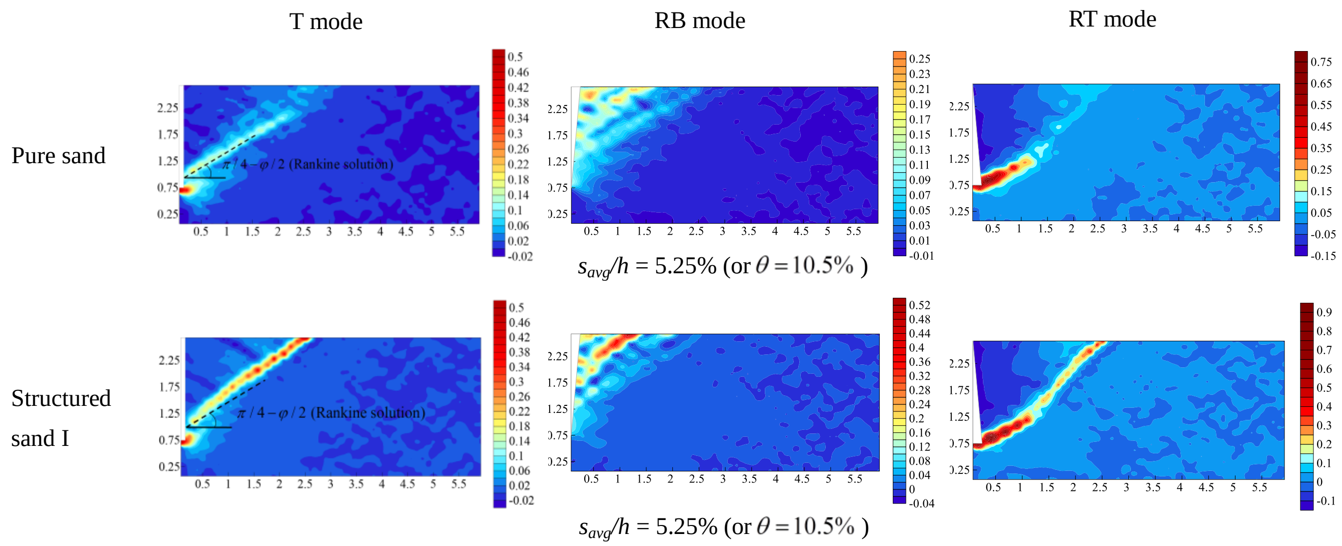

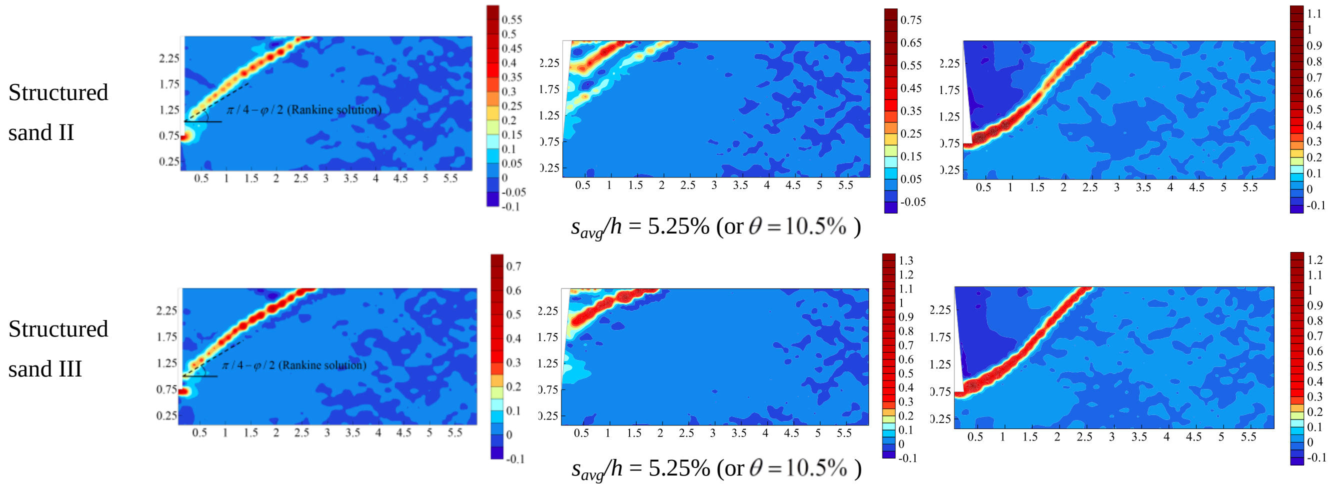

(b) Four sand cases at s_{avg}/h = 5.25% (or $\theta = 10.5\%$ at rotation movement modes) by DEM modelling

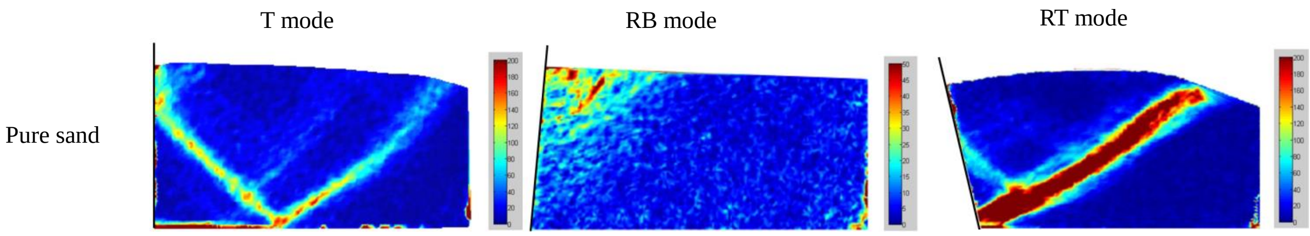

(c) Experimental results in initially dense pure sand with s_{avg}/h = 6.94% [32]

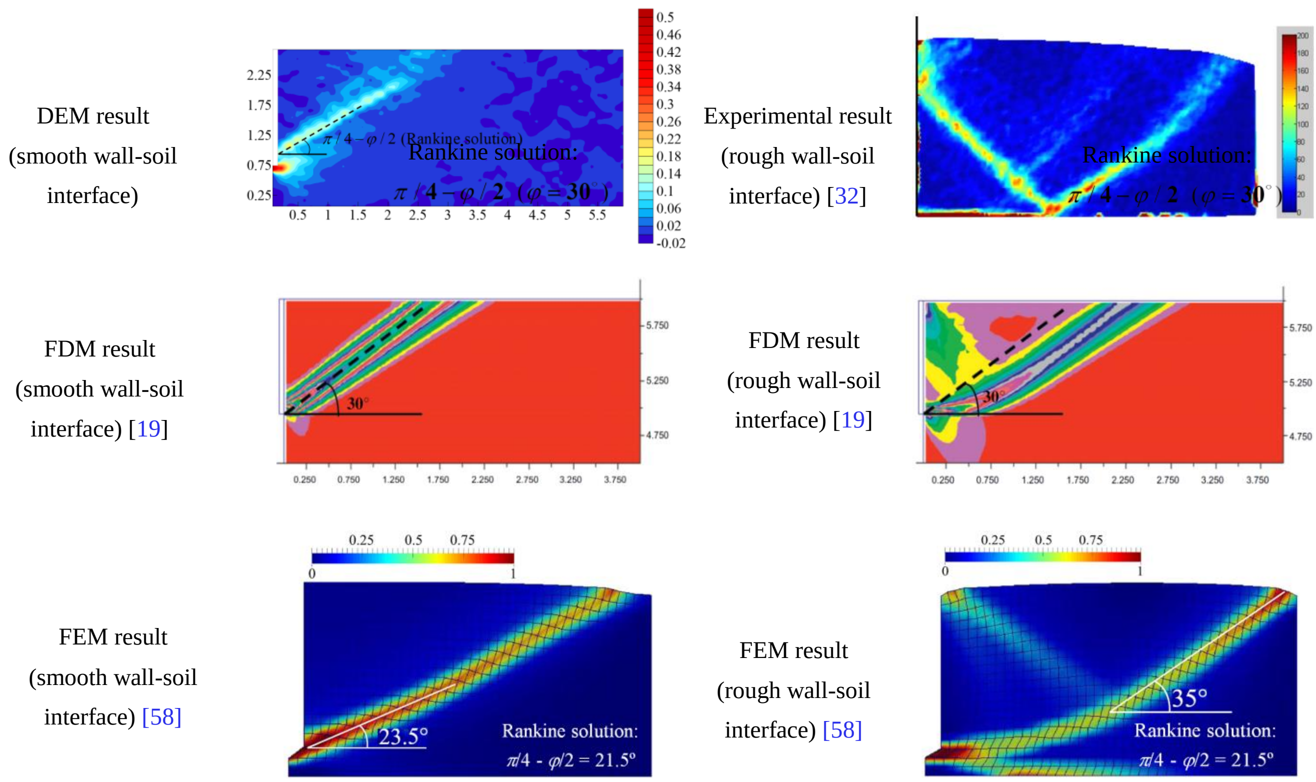

(d) Effect of wall-soil interface roughness on the shear strain contours in pure sand at the T mode

Fig.4 Contours of shear strain in different cases by numerical simulations and experiments

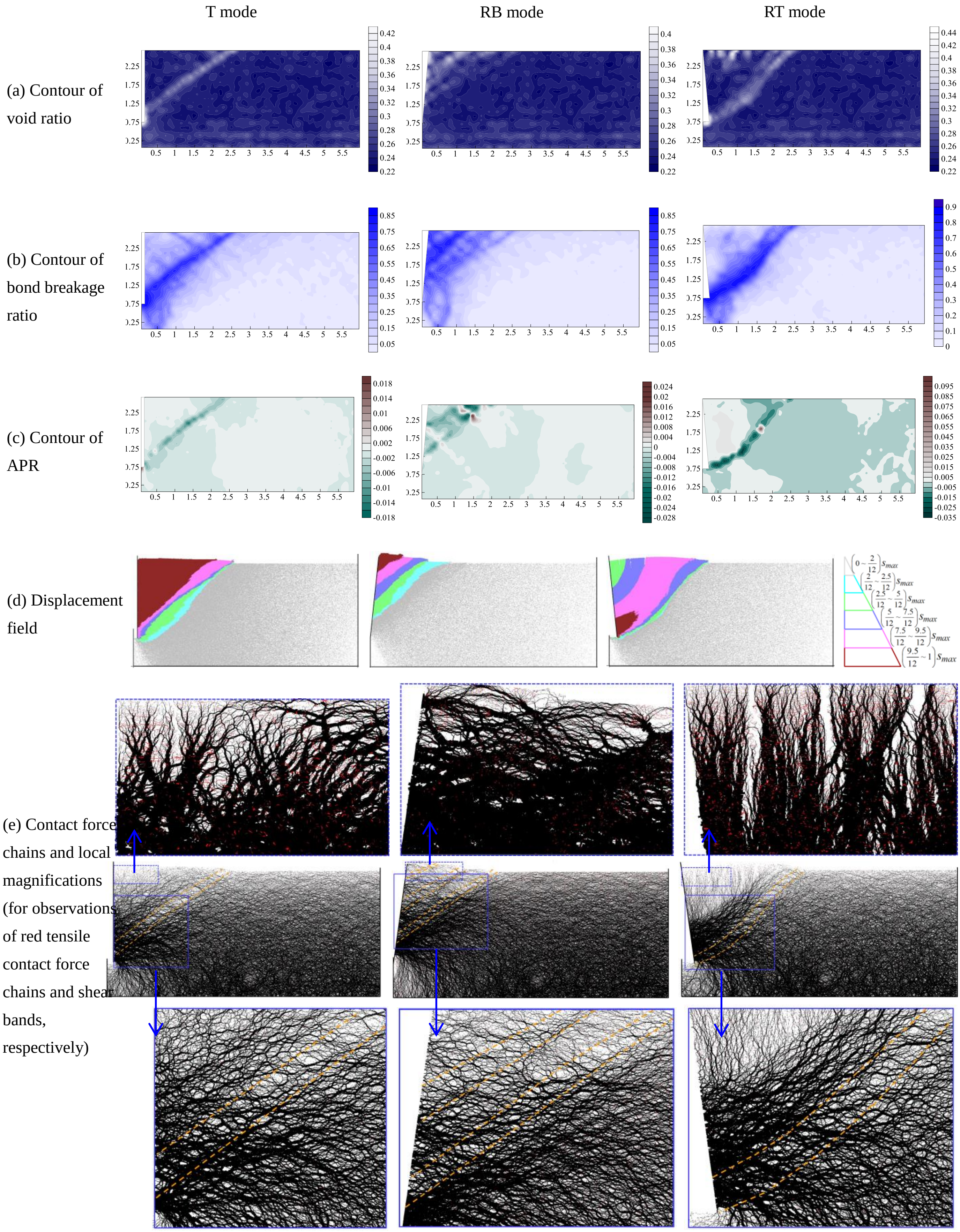

Fig.5 Related distributions in structured sand I case at s_{avg}/h = 5.25% (or $\theta = 10.5\%$ at rotation movement modes).

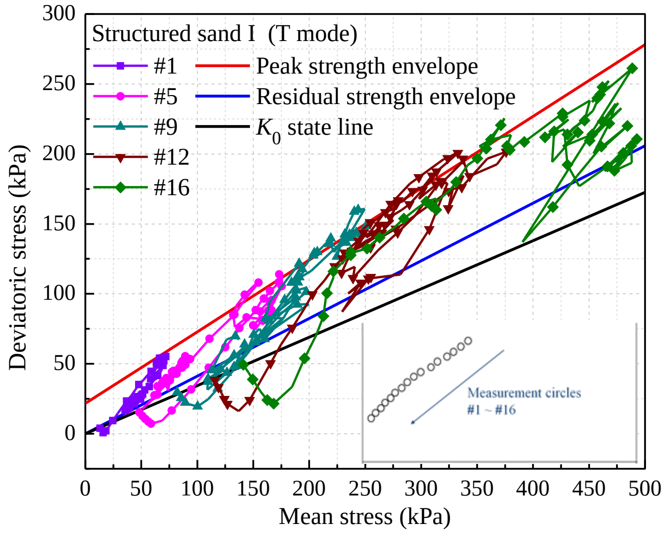

(a) At the T mode

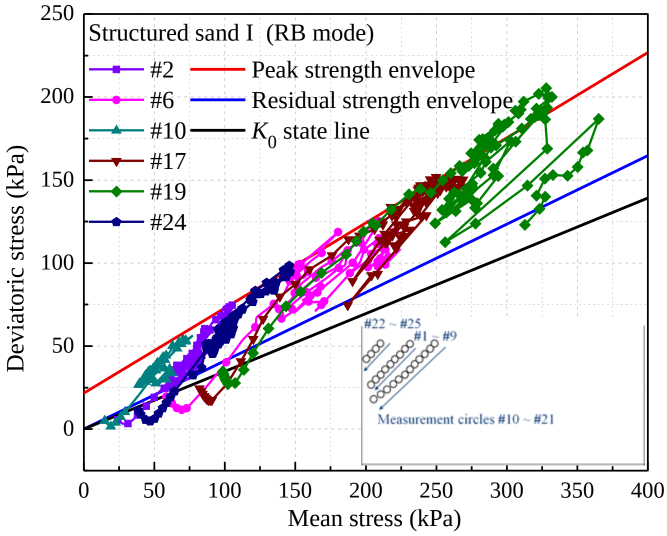

(b) At the RB mode

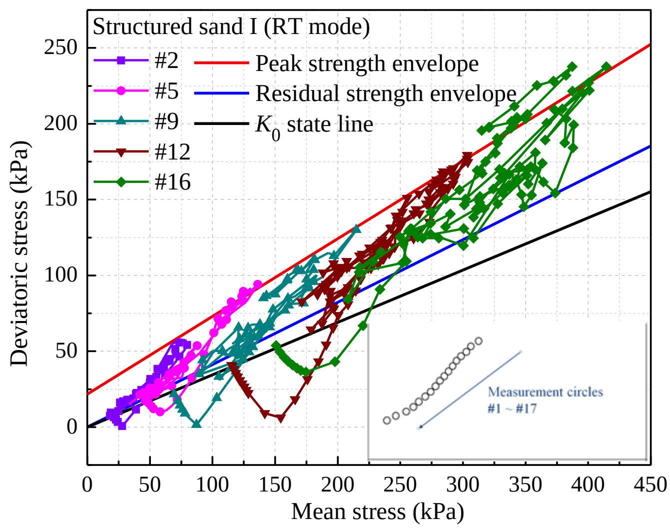

(c) At the RT mode

Fig.6 The traced stress paths of shear bands in structured sand I

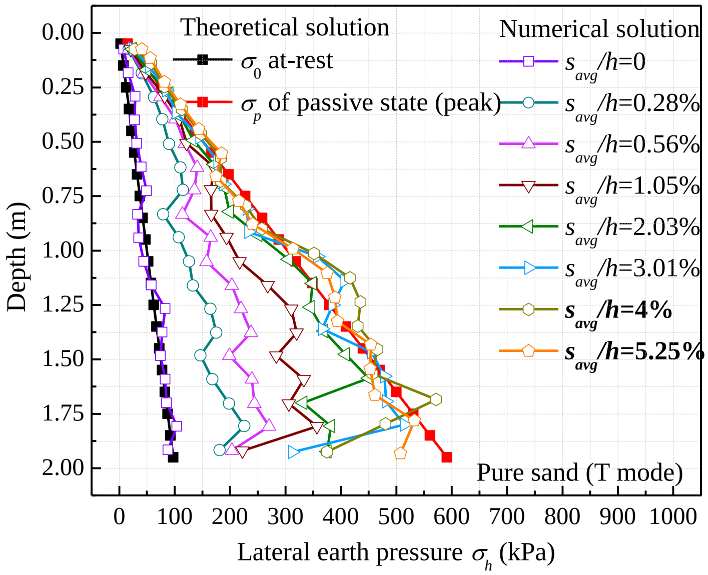

(a) In pure sand case

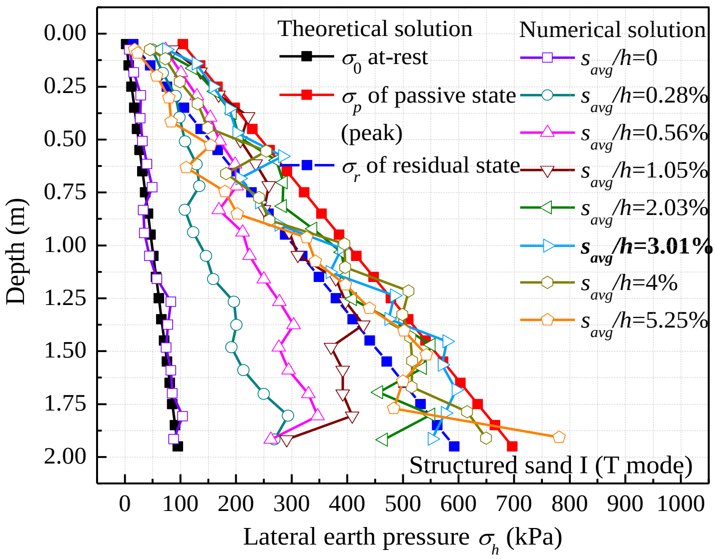

(b) In structured sand I case

Fig.7 Distribution of lateral earth pressure σ_h at different values of s_{avg}/h at the T mode

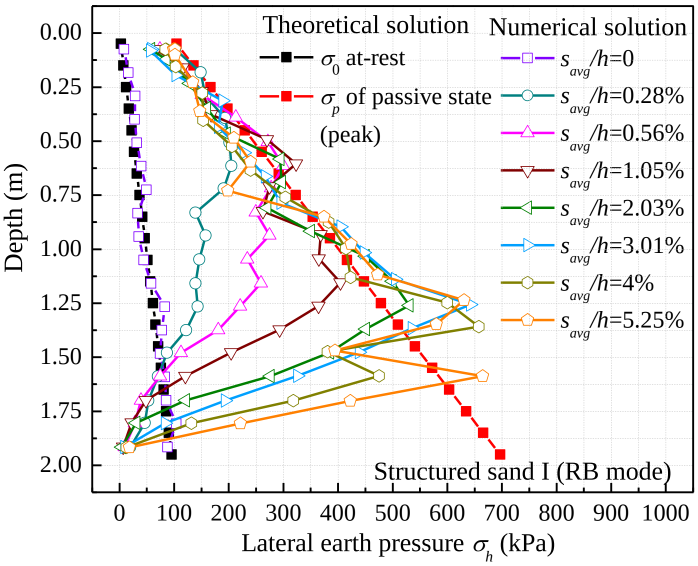

(a) At the RB mode

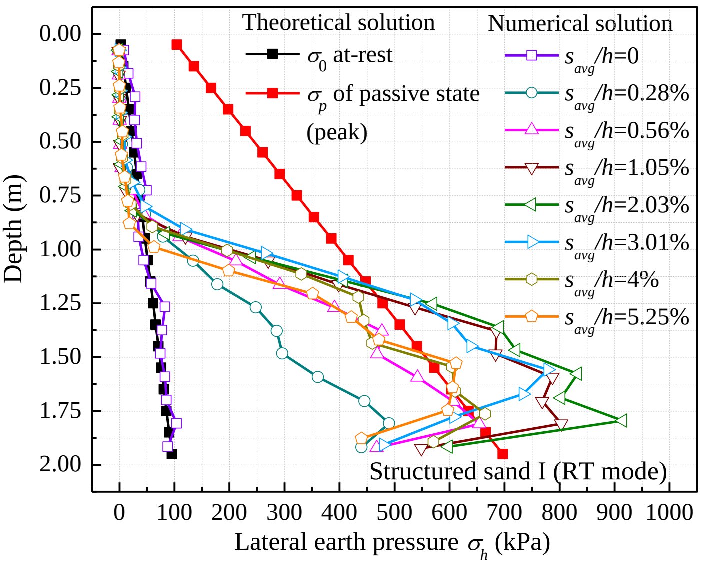

(b) At the RT mode

Fig.8 Distribution of lateral earth pressure σ_h at different values of s_{avg}/h in structured sand I case

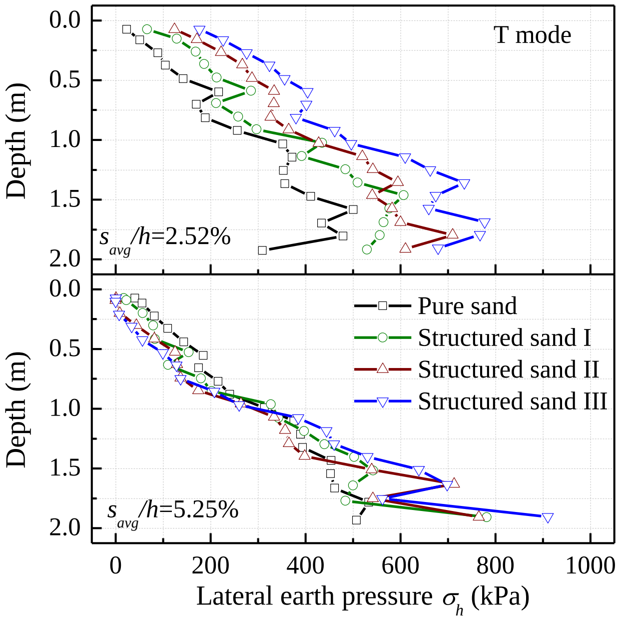

(a) At the T mode

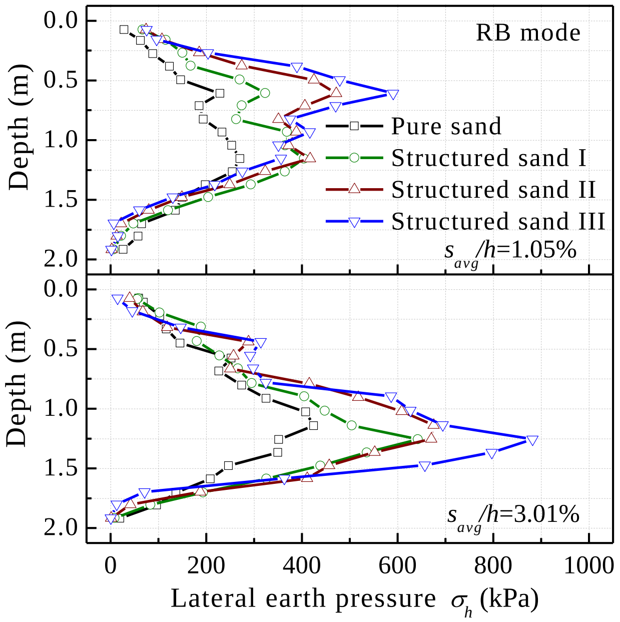

(b) At the RB mode

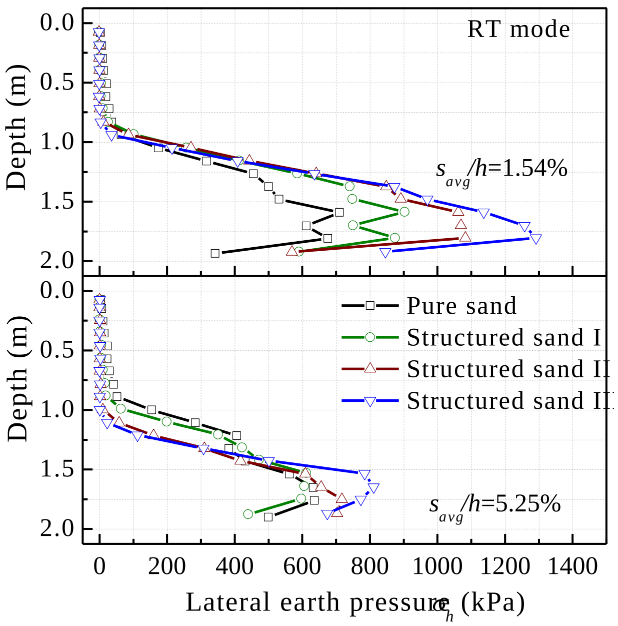

(c) At the RT mode

Fig.9 Comparisons on lateral earth pressure distributions at certain values of s_{avg}/h among all sand cases

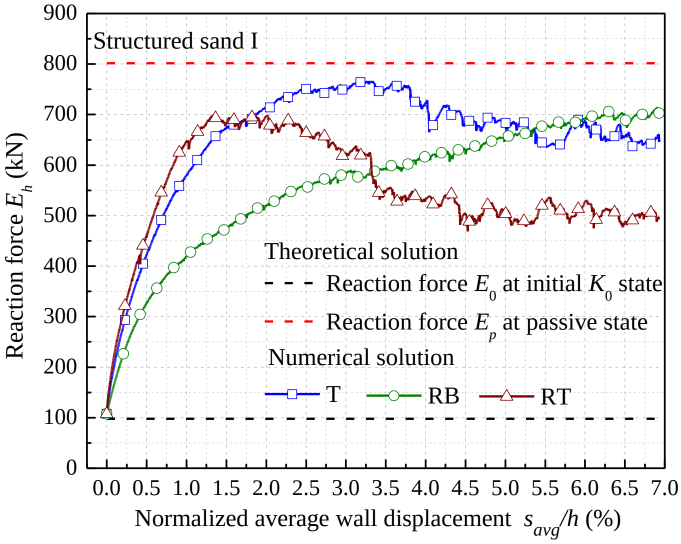

Fig.10 Evolutions of E_h against s_{avg}/h in structured sand I case

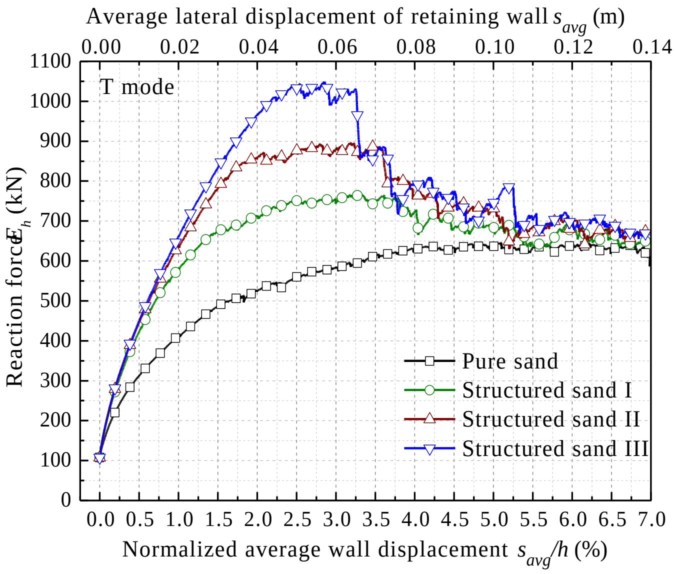

(a) At the T mode

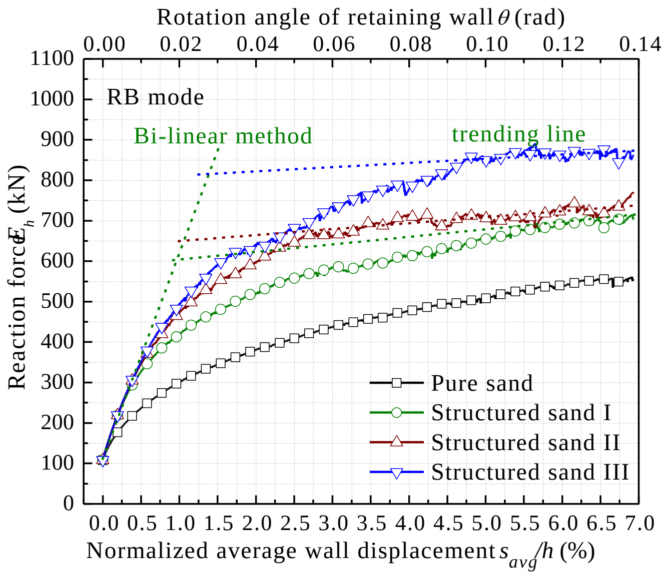

(b) At the RB mode

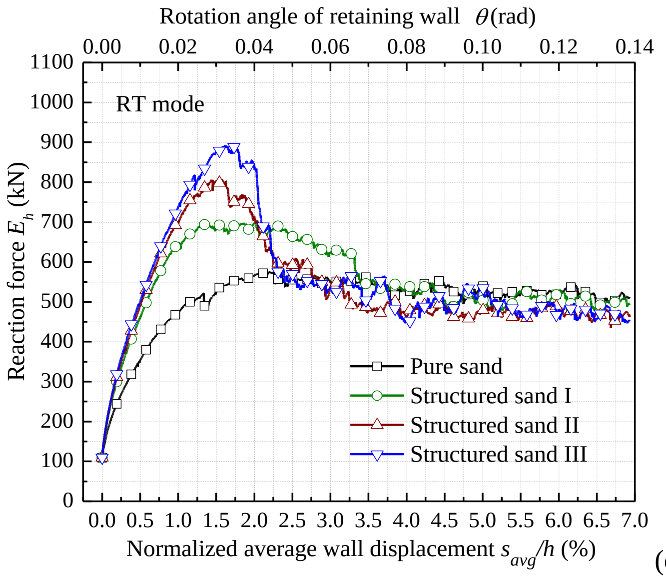

(c) At the RT mode

Fig.11 Evolutions of E_h with s_{avg}/h in all sand cases

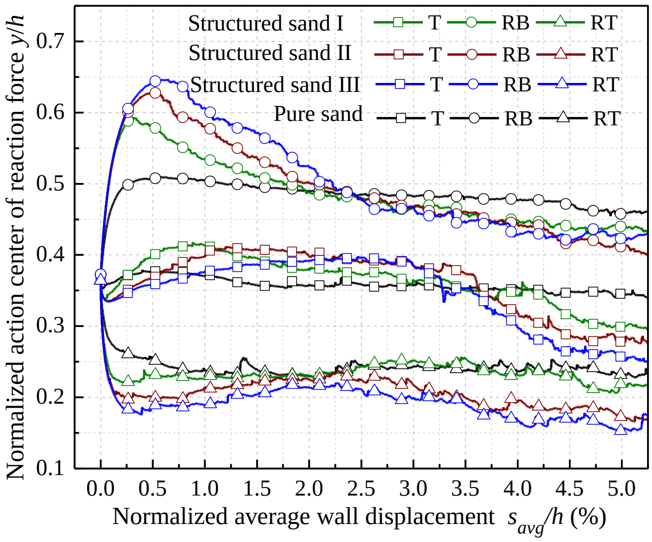

Fig.12 Evolutions of normalized reaction force center *y/h* in all sand cases

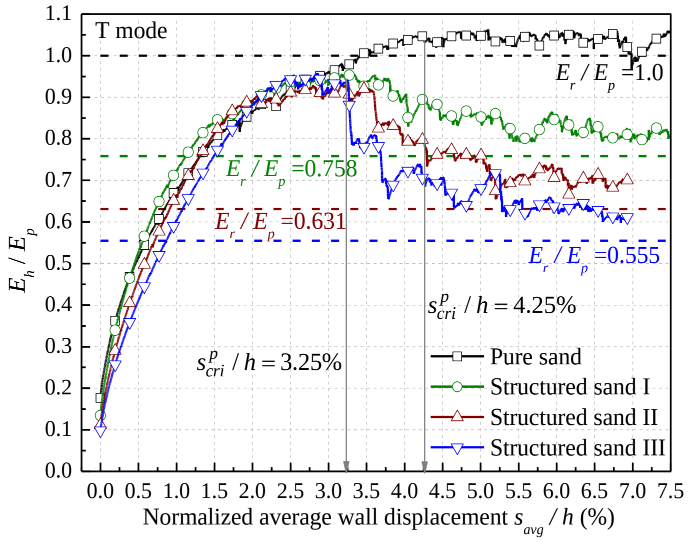

(a) Numerical reaction force E_h normalized by theoretical E_p (Rankine solution)

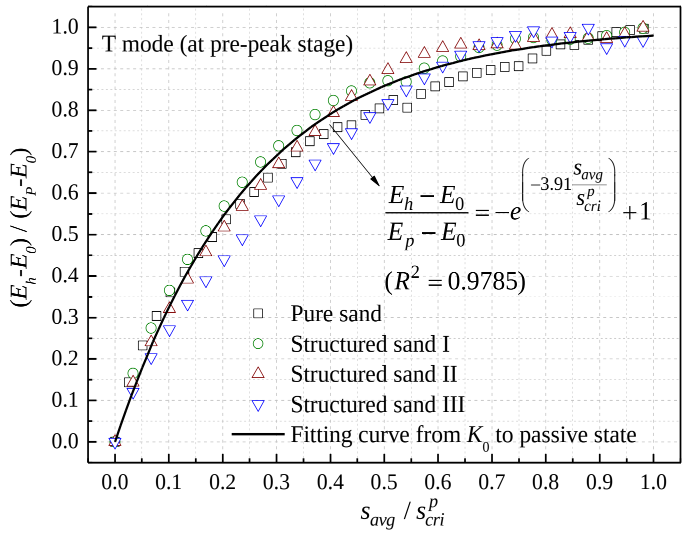

(b) Exponential fitting of normalized reaction force for the pre-peak stage

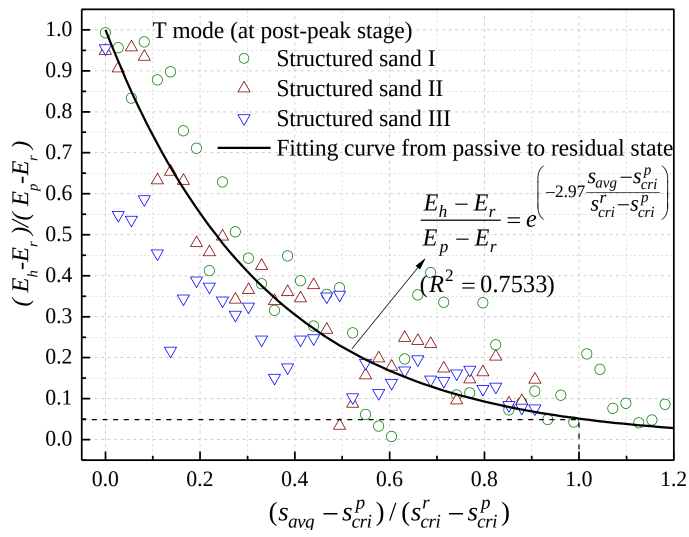

(c) Exponential fitting of normalized reaction force for the post-peak stage

Fig.13 The numerical data of normalized reaction force and fitting curves at the T mode

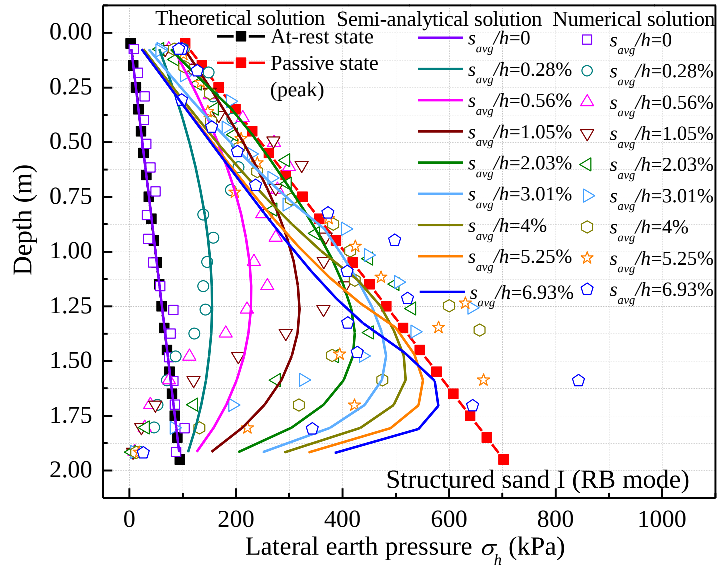

(a) Distribution of σ_h at different values of s_{avg}/h at the RB mode

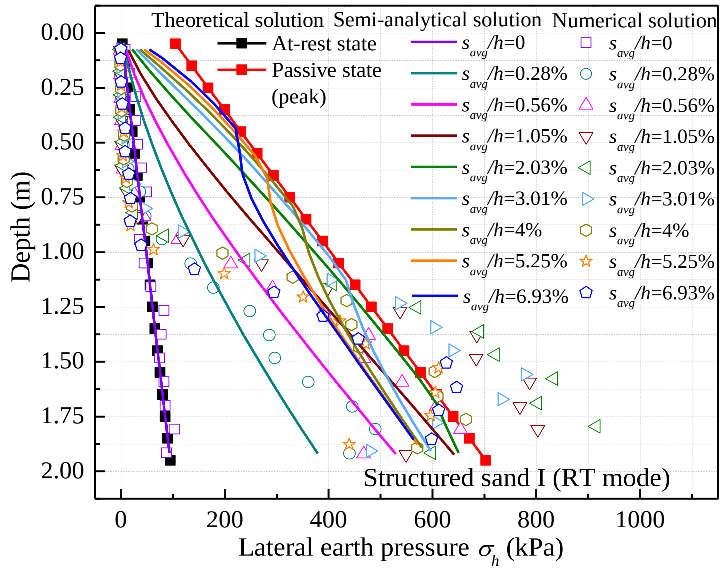

(b) Distribution of σ_h at different values of s_{avg}/h at the RT mode

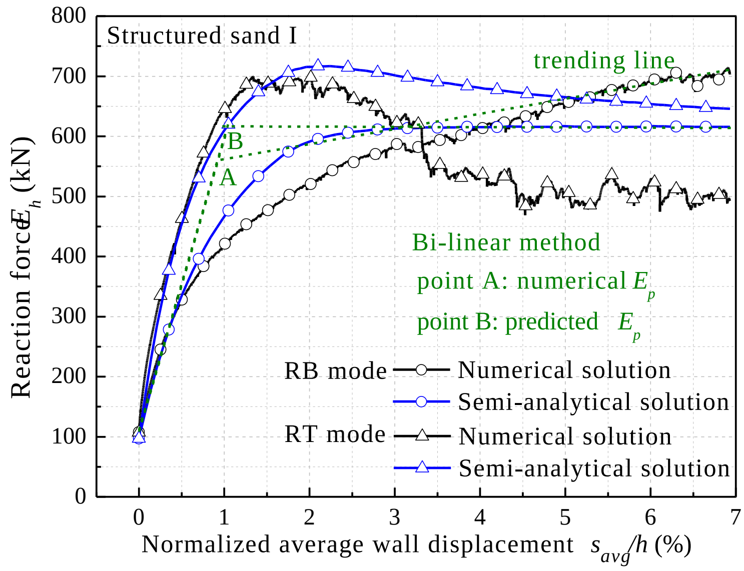

(c) Evolutions of E_h against s_{avg}/h at the RB and RT modes

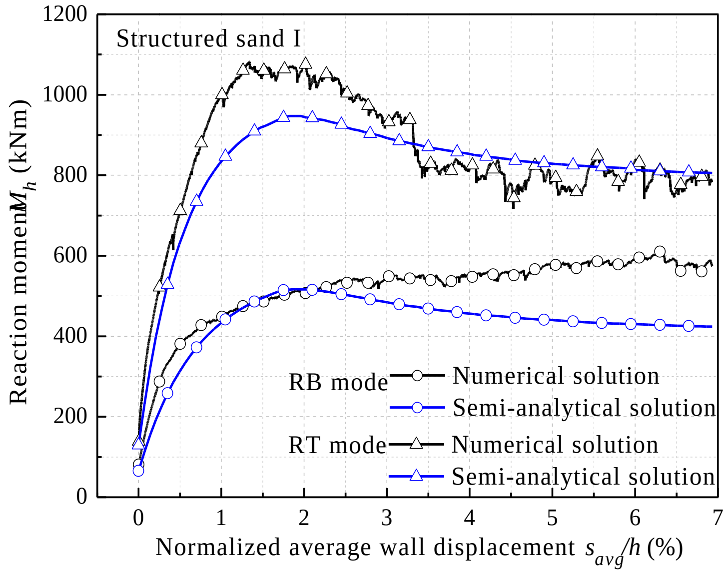

(d) Evolutions of M_h against s_{avg}/h at the RB and RT modes

Fig.14 Comparisons on the numerical results and proposed semi-analytical solutions in structured sand I at the RB and RT modes

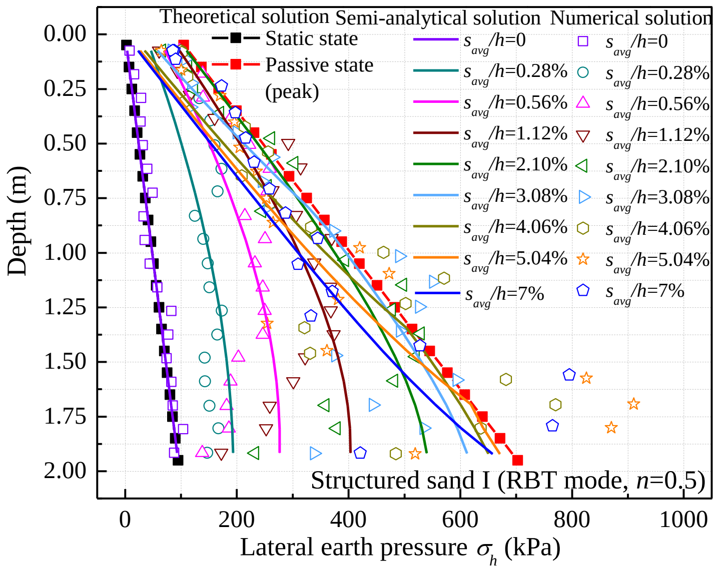

(a) Distribution of σ_h at different values of s_{avg}/h at the RBT mode

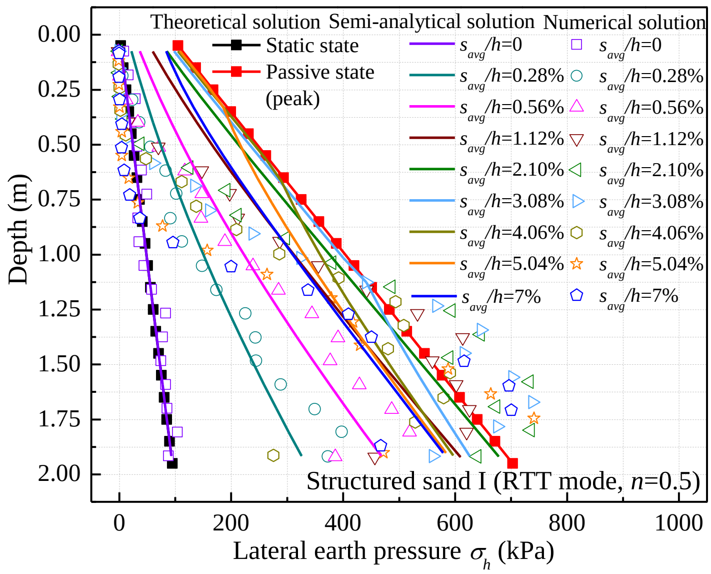

(b) Distribution of σ_h at different values of s_{avg}/h at the RTT mode

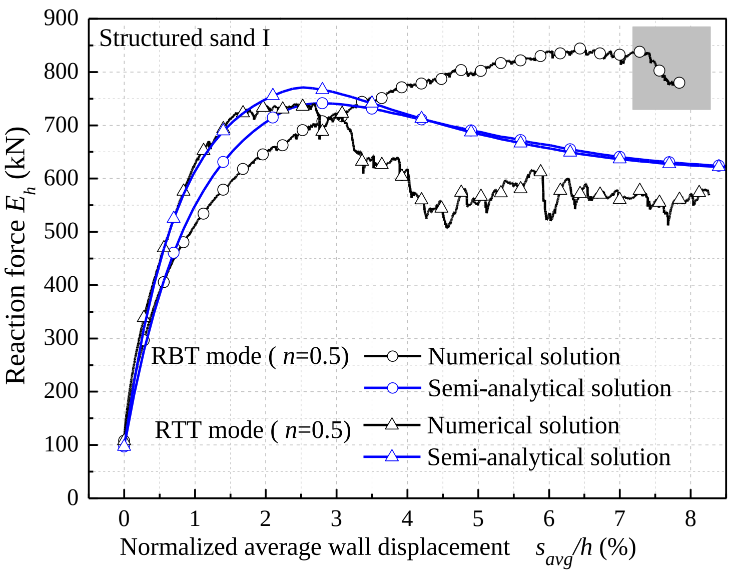

(c) Evolutions of E_h against s_{avg}/h at the RBT and RTT modes

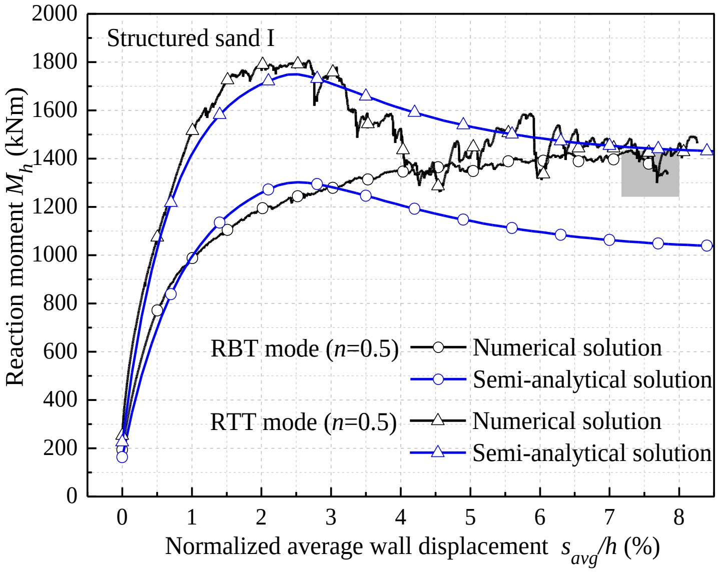

(d) Evolutions of M_h against s_{avg}/h at the RBT and RTT modes

Fig.15 Comparisons on the numerical results and proposed semi-analytical solutions in structured sand I at the RBT and RTT modes with n = 0.5

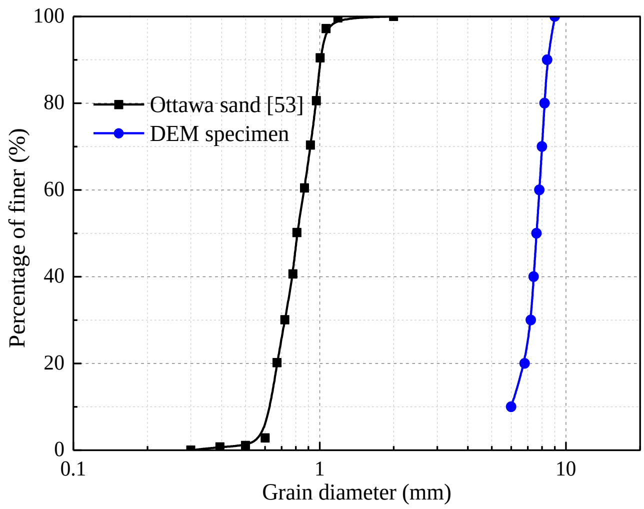

(a) Particle size distribution for experimenal Ottawa sand and DEM granular material

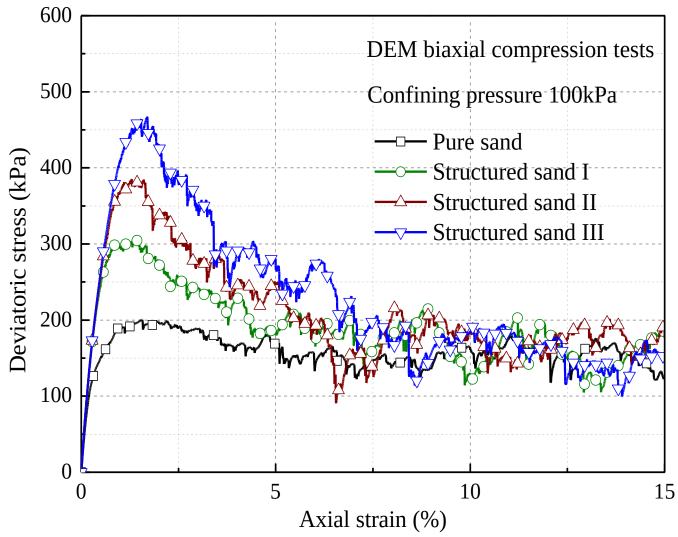

(b) Stress-strain responses of pure/structured sands by DEM biaxial compression tests

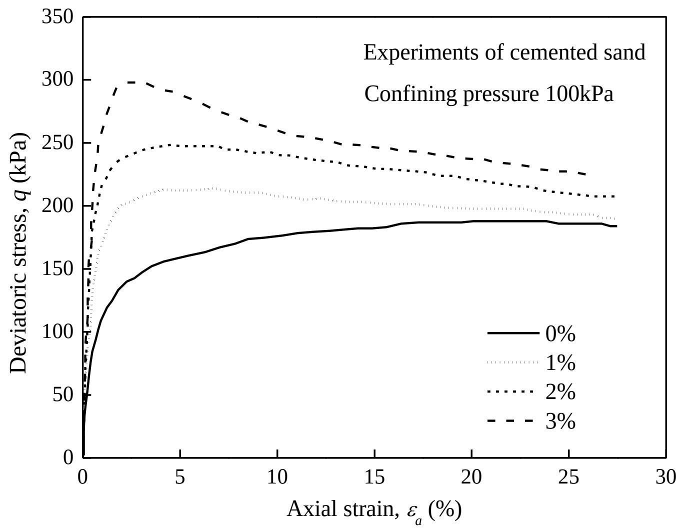

(c) Experimental stress-strain responses of cemented sands [53]

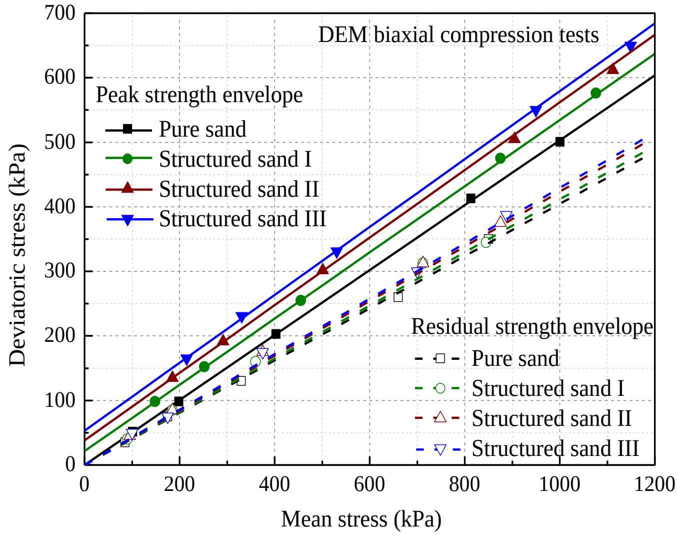

(d) Peak/residual strength envelopes of pure/structured sands by DEM biaxial compression tests

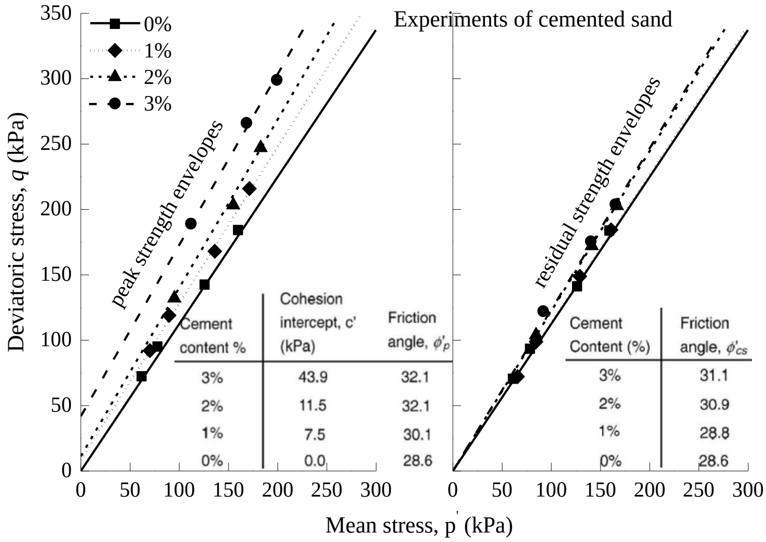

(e) Experimental peak/residual strength envelopes of cemented sands [53]

Fig. 16 Properties of the used granular materials through DEM elementary tests in comparison with experiments by Wang and Leung [53]